Carbon nanotube based biosensor for high sensitivity and dual mode measurement

Jeseung Oh

The Graduate School

Yonsei University

Graduate program for Nanomedical Science

Carbon nanotube based biosensor for high sensitivity and dual mode measurement

A Dissertation

Submitted to the Graduate program for Nanomedical Science and the Graduate School of Yonsei University

in partial fulfillment of the

requirements for the degree of

Doctor of philosophy

Jeseung Oh

June 2012

This certifies that the dissertation of

Jeseung Oh is approved.

_____

Thesis Supervisor: Kyung-Hwa Yoo

_____

Thesis Committee Member: In-hong Choi

_____

Thesis Committee Member: Kook Jin Lim

_____

Thesis Committee Member: Hyo-Il Jung

_____

Thesis Committee Member: Jae-Chul Pyun

The Graduate School

Yonsei University

June 2012

감사의 글

먼저 대학원에 진학하고 박사과정까지 진학하여 공부를 할 수 있게 뒤에서 묵묵히 저를 믿어주시고 힘이 되어주신 부모님께 깊이 감사 드립니다. 그리고 저의 동생 제훈이도 고맙다는 말을 하고 싶습니다. 저를 대학원 재학 기간 동안 부족한 저를 위해 많은 조언과 가르침을 주시고 학위 논문을 쓰기까지 이끌어주신 것 정말 감사합니다. 저의 지도 교수님이신 유경화 교수님께도 깊이 감사 드립니다. 그리고 저의 대학원 생활에서의 처음 사수로써 많은 것을 가르쳐주시고 또한 많은 인생공부를 하게 해주신 최향희 박사님 과 방상용 원장님께도 깊이 감사 드립니다. (그리고 선휘 /선우도 고맙다~~)
저의 박사 논문을 심사해주신 임국진 박사님, 의과 대학 면역학 교실의 최인홍 교수님, 기계공학과의 정효일 교수님 그리고 신소재공학과의 변재철 교수님께도 감사 드립니다.

대학원에 다니면서 항상 힘이 되어주고 많은 추억을 만들었던 영욱, 승환, 성인, 민수 그리고 먼저 졸업을 하여 어린 아이들과 치열하게 공부를 하고 있을 희열이, 열심히 직장을 다니고 있는 봉근, 창섭, 정도, 재학도 많이 생각납니다.

학위 과정 동안 많은 것을 배우고 많은 것을 느끼고 이제 사회에 나가 슬기롭게 지낼 수 있게 되었습니다. 앞으로도 학위 과정 동안 배우고 경험한 것을 잊지 않고 열심히 살겠습니다.

CONTENTS

LIST OF FIGURES

ABSTRACT

Carbon nanotube based biosensor for high sensitivity and dual mode measurement

Jeseung Oh

Graduate program for

Nanomedical Science

The Graduate school

Yonsei university

We have fabricated carbon nanotube (CNT)-based biosensors on transparent quartz substrates, which can detect biomolecules by measuring the conductance change and the surface plasmon resonance (SPR). The device has a metal semiconductor field effect transistor (MESFET) structure with a metal (Au) top gate between source and drain electrodes. Since this Au topgate acts as a Schottky metal gate, the conductance of the device is controlled by the metal gate. In order to see whether it is possible to detect biomolecules adsorbed on the Au topgate using the CNT-MESFET, thiol-modified single strand DNA molecules are

immobilized on the Au top gate and then DNA molecules with the complementary base sequence are added. When DNA hybridization occurs, the CNT conductance is observed to decrease, suggesting that biomolecules adsorbed on the Au top gate can be detected by measuring the conductance change. In addition, the Au top gate is also able to be utilized for SPR measurements, which detects the change in refractive index induced by binding of biomolecules on the metal surface. Indeed, we have demonstrated that DNA hybridization can be detected using the CNT-MESFET by measuring the SPR angle shift. Since the sensitivity of biosensors measuring the conductance change is higher than SPR biosensors, whereas the reproducibility and the reliability are better in SPR biosensors. Therefore, this dual mode CNT biosensor is expected to provide high sensitivity reinforced with more reliability.

We compared the sensitivity of CNT-MESFET sensor and CNT-FET sensor using measuring the electrical conductance. CNT-MESFET showed higher sensitivity than the CNT-FET sensor due to the high gate capacitance in aqueous environment and the merit of immobilization biomolecules at Au surface.

Keywords: carbon nanotube, biosensor, field-effect transistor, metal-semiconductor field-effect transistor, dual mode, electrical conductance, surface plasmon resonance, DNA hybridization, hepatitis B

Chapter I

Introduction

1.1. Carbon nanotubes

1.1.1. Carbon nanotube structure

Carbon nanotubes (CNTs), discovered by Iijima, S [1], can be explained as a graphene rolled up into a nanoscale diameter tube. Many investigators have since reported remarkable physical and mechanical properties for new material of carbon. From extraordinary electronic property, thermal conductivity and mechanical property (stiffness, strength and resilience exceeds any current material). Carbon nanotubes offer enormous opportunities for the development of new material.

In addition to the superior mechanical properties of the carbon nanotubes, they also posses exceptional thermal and electric properties: thermally stable up to 2800 °C in vacuum, thermal conductivity about twice as high as diamond, electrical current carrying capacity 1000 times higher than copper wires [2]. These excellent electric properties of carbon nanotubes have been investigated for devices such as field-emission display [3], scanning probe microscopy tips [4], and microelectronic devices [5, 6].

An ideal carbon nanotube can be viewed as a hexagonal network of carbon atoms rolled up to form a hollow cylinder. A single-walled carbon nanotube (SWNT) is single rolled up graphene, whereas a multi-walled carbon nanotube (MWNT) consists of several homocentric cylinders of SWNTs. SWNTs have only a few nanometers in diameter and can grow to be several centimeters long. Such dimensions give rise to aspect ratios (length/diameter) of over ten million. SWNTs can be either metallic or semiconducting. Fig. 1 shows the single-walled carbon nanotube (SWNT), double-walled carbon nanotube (DWNT) and multi-walled carbon nanotube (MWNT).

The properties of nanotubes depend on atomic arrangement, the diameter and length of the tubes, and the morphology or structure. The atomic structure of nanotubes is described the nanotube chirality which is defined by the chiral vector (C_h) and the chiral angle (θ). The chiral vector is defined on the hexagonal lattice as $C_h = na_1 + ma_2$, where a_1 and a_2 are unit vectors, n and m are integers. The chiral vector C_h uniquely defines a particular (n, m) tube, as well as its chiral angle (θ), which is the angle between C_h and a_1 (Fig. 2 (a)).

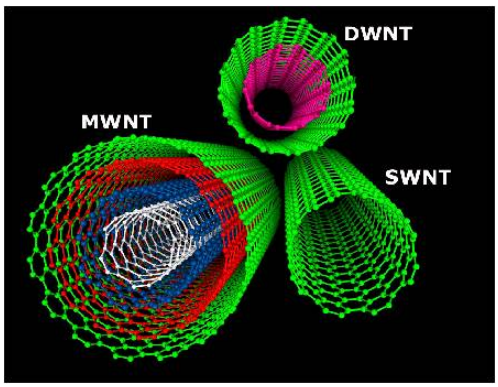

Figure1. A schematic representation of the carbon nanotubes

It can vary between 0 and 30º, which allow obtaining three configurations of CNTs (Fig. 2). Armchair nanotubes formed when $n = m$ and the chiral angle is 30°. Zigzag nanotubes formed when either n or m is zero and the chiral angle is 0°. All other nanotubes, with chiral angles intermediate between 0° and 30°, are known as chiral nanotubes. The difference in zig-zag, armchair and chiral nanotube structure is shown in Fig. 2 (b).

The chirality of the carbon nanotube has significant implications on the material properties. In particular, tube chirality is known to have a strong impact on the electronic properties of carbon nanotubes. Graphite is considered to be a semi-metal, but it has been shown that nanotubes can be either metallic or semiconducting, depending on tube chirality [9].

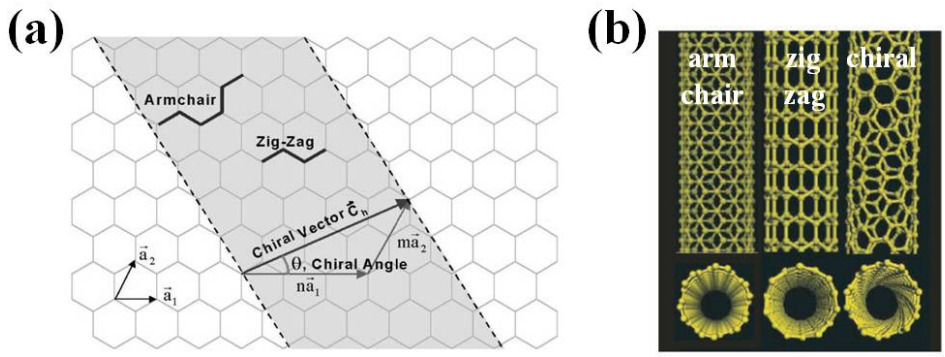

Figure 2. Structure of typical carbon nanotube (a) A Schematic diagram showing how a hexagonal sheet of graphite is rolled to form a carbon nanotube [7]. (b) Illustrations of the atomic structure of an armchair, zig-zag and chiral nanotube [8].

1.1.2. Electrical property

The graphene can be characterized as a zero bandgap semiconductor or a metal, since the density of states (DOS) is zero at the Fermi energy (E_F), and imparts those properties to a nanotube. Carbon nanotube depends on the conducting properties on the nature of chirality and the diameter (SWNTs have diameters in the range 0.4 nm–2 nm) [10]. Carbon nanotube contains sp2-hybridized carbon atoms. Three out of the four outer shell electrons of these carbons participate in bonding with neighbor carbons while the fourth electron is in a p-orbital perpendicular to the hexagonal lattice. In a graphene sheet, these p-

orbital electrons are distributed in the valence (π) and conduction (π*) bands, providing a semi-metallic character owing to their theoretically zero bandgap.

According to the energy band model, carbon nanotube is possible to distinguish between metallic, semiconductor and insulator by considering whether conductivity and valence band are separated by a bandgap. An electron is required the energy to move from the valence band to the conduction band. In the case of insulator materials energy gap (E_g) is higher than ~5 eV. Semiconducting nanotubes energy band gap is lower than ~ 5 eV but has a dependence on the diameter. In the case of smaller diameter carbon nanotubes have larger band gaps. An occasion of metallic nanotubes there is no gap between the valence band and the conduction band. To classify of CNTs in metallic and semiconducting, another important parameter is the position of the Fermi energy with respect to the charge neutrality point (CNP). For an undoped CNT the E_F coincides with the CNP (E_F = 0). Electron or hole doping cause shift of the Fermi energy up or downwards in the energy gap. If the doping induced Fermi level shifts are larger than the energy separation between the one-dimensional sub-bands, a semiconducting CNT is turned into a metallic one.

Mintmire [11], Hamada [12], and Saito [13] predicted through tight binding of electronic structure calculations that the relationship between the coefficients (n_1 and n_2) of the chiral vector ($C_h = n_1a_1 + n_2a_2$) determines the conducting properties (Fig. 2). When $2n_1 + n_2$ is an integer multiple of three, the CNT exhibits metallic behavior. If all values of the chiral vectors were equally probable, it would be expected that 1/3 of the total SWNTs would be metallic while the remaining 2/3

would be semiconducting, which is indeed what is found in synthesis [10].

The Fermi level crossing for zig-zag (n_1, 0) tubes, which can be metallic or semiconducting, is at the center of the Brillouin zone (k = 0). However, for armchair (n_1, n_1) tubes, the level crossings are at $k = \pm \frac{2\pi}{3a0}$ and they are always metallic. It has also been found that for all metallic nanotubes, the E_F intersects two bands of the one dimensional band structure. (This contributes a kinetic inductance to the nanotube, which has implications in the high frequency electronic properties of nanotubes [14]).

As can be seen from Fig. 2, the nanotube diameter (d_t), dictated through C_h, also affects the electron dispersion and it was derived [15] in a semiconducting nanotube ($E_g = \frac{4\hbar vF}{3dt}$). The influence of the band structure topology (E_k) on the conduction is manifested through the relationship for the Fermi velocity ($\upsilon_F = \hbar^{-1}\Delta_k \cdot E_k$). The above translates numerically [16] to $E_g = \frac{0.9}{dt}$ eV, with a $\upsilon_F \sim 10^6$ m/s. The electronic structure, as represented through a density of states (DOS) diagram is found to exhibit characteristic ($E^{-1/2}$) van Hove type singularities - typical of a one dimensional system, was well manifested in electrical [17] and optical measurements. In the case of metallic nanotubes have the zero DOS. However, the DOS of semiconducting nanotube is finite.

For semiconducting SWNTs the Fermi energy (E_F) is taken to be at a reference value of zero. However, for a realistic graphene based carbon nanotube doping is inevitable due to the presence of adsorption material from the ambient environment, which would cause charge transfer. In that case, the E_F is either <0

(for hole doping, electron transfer from the nanotube - p type) or >0 (for electron doping, electron transfer to the nanotube - n type). The effects of temperature also have to be taken into consideration i.e., (i) $k_BT > E_F$ or (ii) $k_BT < E_F$. Case (i), suitable for high temperatures, corresponds to low doping while low temperatures (case (ii)) are typify strong doping conditions.

When connected to external contacts, semiconducting SWNTs are usually measured p-type characteristics. This characteristic could be induced by the higher work function of the contact material [18] whereby holes could be generated in the nanotube due to electron transfer from the nanotube to the contact. However, in top-gate device with a field effect transistor (FET), that device can show ambipolar characteristics [19] with large drive currents. The device characteristics are then determined by the relative heights of the Schottky barrier for electron-hole injection at the metal-CNT interface. It was also determined that the annealing in vacuum [20] which results in a shift in the Fermi energy from the valence band to mid-gap. Exposure to oxygen resulted in reversion to p-type characteristics. Evidence for charge transfer in doped carbon nanotubes exposed to electron donor (K, Rb) and electron acceptor (Br, I) atoms was also seen through Raman spectroscopy investigations through a vibration mode shift [21].

It is seen that intrinsic nanotubes cannot be produced whenever there is exposure to oxygen ambient. The effect of oxygen on nanotubes is plausibly not just due to doping, as is conventionally understood but could be related more to the effects on the contacts.

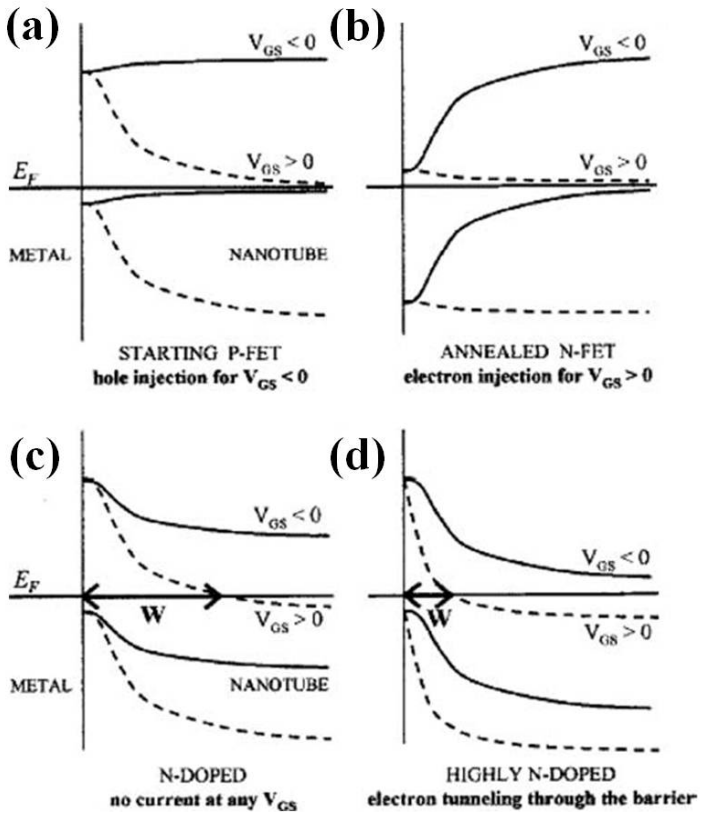

Figure 3. Schematic energy band diagram in the region of the metal-nanotube contact at V_{DS} = 0. (a) the doping is p-type due to the higher work function of the metal and extrinsic oxygen doping, (b) When oxygen is driven out through an annealing treatment, the transistor behavior mimics a n-doped device in that electron injection is allowed (c) n-type behavior is only obtained through alkali element doping, (d) At higher doping levels, electron tunneling occurs through a thin barrier [19].

Also, the absorption [22] of the oxygen with CNTs is weak and is unlikely to result in charge transfer. A phenomenological model was advanced to explain the p-

to n-conversion (Fig. 3), where the concentration of oxygen is proportional to, and determines the position of, the E_F at the metal-CNT interface. Such an effect changes the line-up of the bands at the interface but does not involve the bulk of the CNT.

When E_F at the junction is close to the center of the band gap, the barrier allows tunneling and ambipolar transport is observed. With Au contacts in air, only holes can be injected into the device, while removal of oxygen results in only electrons being injected due to the high hole injection barriers (Fig. 3 (b)). Subsequently, exposing the CNTs to nitrogen [23] and alkali metal dopants [20] resulted in n-doping. However, in the latter case the strong oxidizing characteristics of the dopant are undesirable and stable doping can instead be obtained through functionalization by amine-rich polymers [24] such as polyethyleneimine (PEI).

1.1.3. Synthesis of carbon nanotubes

Primary synthesis methods for single and multi-walled carbon nanotubes include arc discharge [25], gas-phase catalytic growth from carbon monoxide [26], and chemical vapor deposition (CVD) from hydrocarbons [27-29], laser ablation [30] methods.

- Arc discharge

The arc discharge method was the first technique used to produce carbon nanotubes. The arc discharge method was the same method to synthesize fullerene molecules. In Fig. 4 is the illustration of the arc discharge apparatus, the arc discharge technique generally involves the use of two high purity graphite rods as the anode and cathode. The principle of this technique is to vaporize carbon in the presence of catalysts under reduced atmosphere of inert gas (argon or helium). After the triggering of the arc between the anode and cathode, a plasma is formed consisting of the mixture of carbon vapor, the rare gas (helium or argon) and the vapors of catalysts. The exact process variables depend on the size of the graphite rods. As the anode is consumed, a constant gap between the anode and cathode is maintained by adjusting the position of the anode.

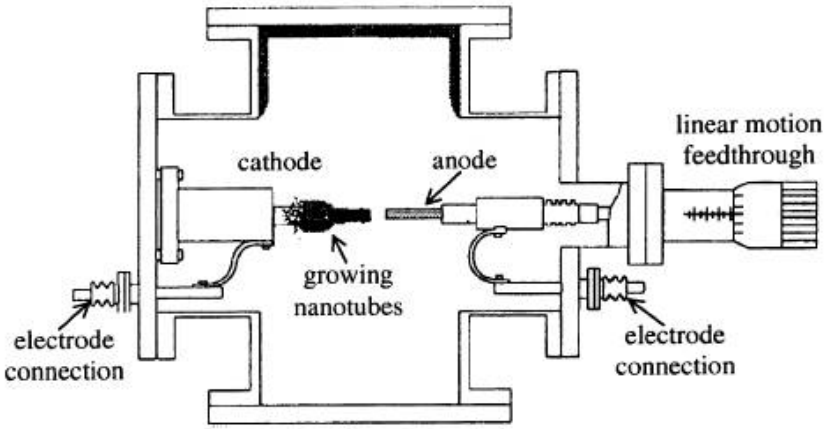

Figure 4. A schematic illustration of the arc-discharge technique system [7]

The vaporization is the consequence of the energy transfer from the arc to the anode made of graphite doped with catalysts. The anode erosion rate is more or less important depending on the power of the arc and also on the other experimental conditions. It is notable that high anode erosion does not necessarily lead to a high of carbon nanotube production. It consists of a cylinder of about 30 cm diameter and about 1m height, equipped with diametrically opposed sapphire windows located so that they face the plasma zone in view of observing the arc. The reactor possesses two valves, one for carrying out the primary evacuation (0.1Pa) of the chamber, the other permitting it to fill with a rare gas up to the desired working pressure. In the arc discharge method, a DC bias of 20–30 V is applied between two carbon electrodes in a helium atmosphere. Carbon atoms are ejected from the anode, and accumulate in the form of nanotubes on the cathode. The electrodes are typically 5–20 mm diameter. To achieve single walled nanotubes, the electrodes are doped with a small amount of metallic catalyst particles (iron, nickel, cobalt, yttrium, boron, gadolinium, and so forth) [31-34]. MWNTs do not need a catalyst for growth. MWNTs can be obtained by controlling the pressure of inert gas in the discharge chamber and the arcing current.The by-products are polyhedron shaped multi-layered graphitic particles in case of MWNTs. As- grown carbon nanotube`s quantity and quality, such as lengths, diameters, purity and etc. of the nanotubes obtained depend on various parameters such as the metal concentration, inert gas pressure, type of gas, plasma arc, temperature, the current and system geometry.

- Laser ablation

Laser ablation was first used for the initial synthesis of fullerenes. The laser ablation technique has been improved to allow the production of single-walled nanotubes [35, 36]. In this technique, a laser is used to vaporize a graphite target held in a controlled at temperatures near 1200 °C. The general system for laser ablation is shown in Fig. 5. During laser vaporization, a graphite target is placed in the middle of a quartz tube mounted in a furnace. To produce SWNTs, the graphite target was doped with cobalt and nickel catalyst [37]. The condense material is then collected on a water-cooled target.

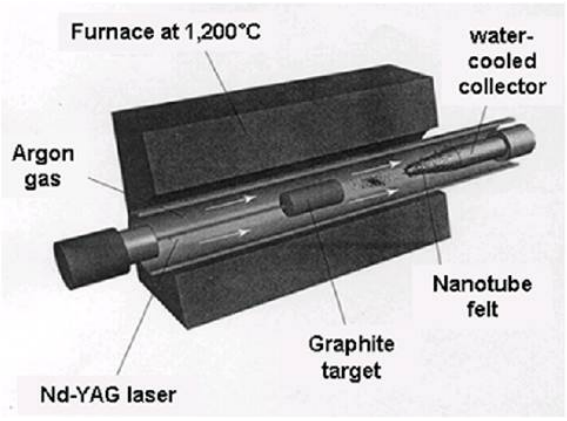

Figure 5. A scheme of the laser-ablation set-up [36]

Nanotubes develop on the cooler surfaces of the reactor as the vaporized carbon condenses. A water cooled surface may be included in the system to collect the nanotubes. The laser ablation method yields around 70% and produces single-

walled carbon nanotubes with a controllable diameter determined by the reaction temperature. However, it is more expensive than either arc discharge or chemical vapor deposition.

Both the arc-discharge and the laser-ablation techniques are limited in the volume of sample they can produce in relation to the size of the carbon source (arc discharge: anode and laser ablation: target). In addition, subsequent purification steps are necessary to separate the tubes from undesirable by-products.

- Chemical vapor deposition (CVD)

In the CVD method, carbon nanotubes are formed by the decomposition of a carbon containing gas. The gas phase techniques are conformable to continuous processes since the carbon source is continually replaced by gas flow. In addition, the final purity of the as-produced nanotubes can be high, minimizing subsequent purification steps.

CVD method employs a carbon source (carbon monoxide, acetylene, methane, etc) which is decomposed in a furnace by heating at temperatures in the range of 500 to 1100 ºC. The carbon released by the decomposition of the gas, carbon is deposited onto the surface of the catalyst particles (usually Ni, Fe and Co) which act as seeds to nucleate the growth of CNT.

Depending on the operating conditions (temperature, catalyst, flow rate of gases, size of the particles) single-walled nanotubes (SWNTs) or multi-walled carbon nanotubes (MWNTs) can be obtained [38-41]. SWNTs are synthesized at higher temperatures (800 - 1100 ºC) than MWNTs. One unique aspect of CVD

techniques is its ability to synthesize aligned arrays of carbon nanotubes with controlled diameter and length.

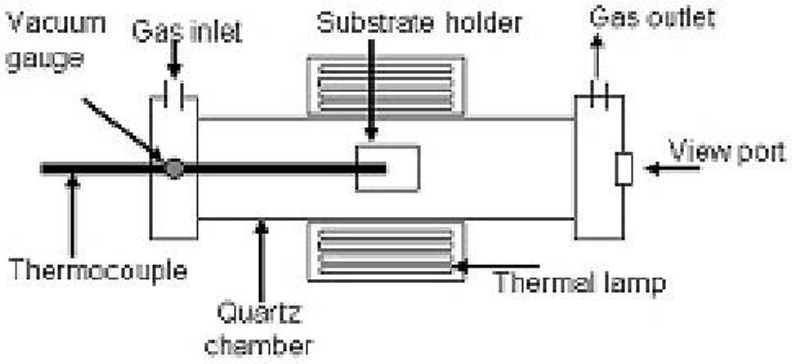

Figure 6. Scheme of the thermal chemical vapor deposition set-up [37]

The synthesis of straight carbon nanotubes on a variety of substrates has been accomplished by the use of plasma enhanced chemical vapor deposition (PECVD) where the plasma is excited by a DC source [27, 28] or a microwave source [42-46].

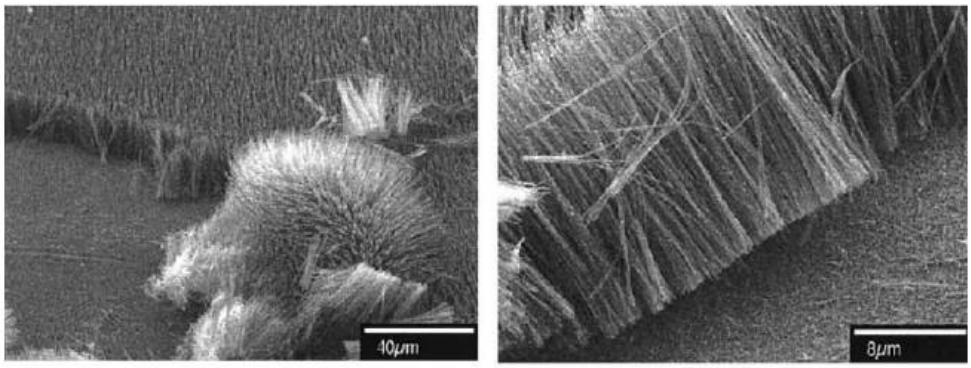

Figure 7. SEM images showing the straightness of MWCNTs grown via PECVD [28]

Fig. 8 shows the ability to grow straight carbon nanotubes over a large area with uniformity in diameter, length, straightness, and density. Adjusting the thickness of the catalyst layer controls the diameter of the tubes, shown in Fig.8.

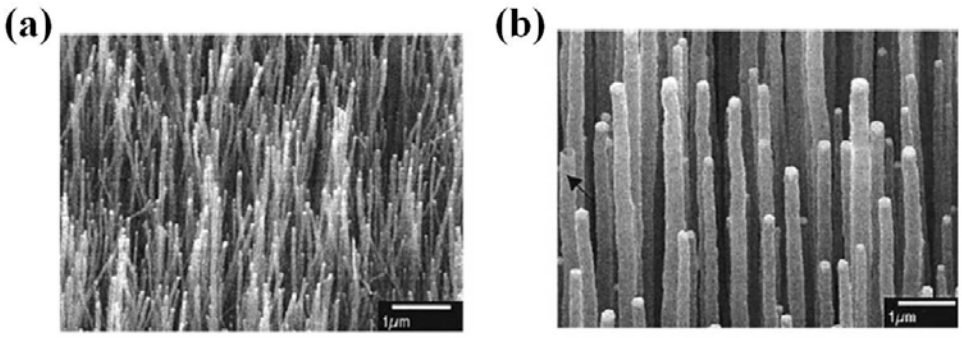

Figure 8. SEM images showing control over the nanotube diameter: (a) 40–50 nm and (b) 200–300 nm aligned carbon nanotubes [28]

1.2. Biosensor

1.2.1. Principle of biosensor

Biosensor technology has grown at such a rapid rate that several new sensors used to interrogate the human body have been developed and today are in high demand. Overall, this situation has created a rapidly rising demand for new noninvasive and in vitro sensor technologies to speed up testing.

A biosensor is an analytic device which is used for the detection of an analyte (i.e. a chemical substance being measured in an analytical procedure) by using a biological material. The analyte combines a biological material with a physicochemical detector component. Biosensors consist of three basic components as shown in Fig. 9, a bioreceptor, a transducer or the detector element and a biosensor reader for data display or acquisition of the results in a user-friendly way.

First, biological element, i.e. biorepector, are the key of the biosensor selectivity, because this part is designed for recognizing the target materials, such as nucleic acid, antibodies, microorganisms, cell receptors, enzymes, and tissue. It is the sensitive part of the bio molecules or analyte interact at this part. Second is a transducer or detector element. This part converts the recognition event into a measurable signal. The transducer or detector element transforms the signal

resulting from the interaction of the analyte with the biological element into another signal that can be more easily measured and quantified. The transducer or detector element parts are mainly concerned with the sensitivity of the biosensor. It works in a physicochemical signal (optical, piezoelectric, electrochemical, thermometric or magnetic).

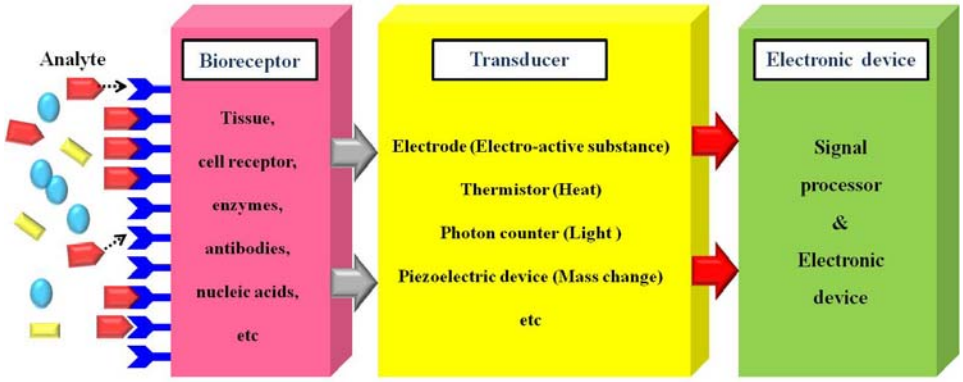

Figure 9. Basic structure of biosensor

The last part of the biosensor is the associated electronics or signal processors that are primarily responsible for the display of the results. Real-time monitoring is necessary on the biosensor measurement step. For the real-time monitoring, associated electronics or signal processors collect and analyze the measured data. The appropriate choice of the electronic device and signal processor can generate an easy display for the real-time monitoring.

1.2.2. Carbon nanotue based FET biosensor

Most biological sensing techniques rely largely on optical detection principles. These techniques are highly sensitive and specific but are inherently complex, for they involve multiple steps between the actual engagement of the analyte and the generation of a signal. These techniques require multiple reagents, preparative steps, signal amplification, and complex data analysis. Electronic detection, utilizing nanoscale devices, offers advantages for two reasons. The first is size compatibility. Recent advances in nanoscale materials, we are now able to construct electronic devices in which the component parts are comparable in size to biological entities, thus ensuring appropriate size compatibility between the detector and the detected species. Some length scales in Fig. 10 illustrate this observation (single cells are approximately 1 μm, viruses are approximately 100 nm, proteins are on the order of 10 nm, and the diameter of the DNA duplex is approximately 1nm). The diameter of single-wall carbon nanotubes is in the 1 nm range, the diameter of the DNA duplex.

The second advantage is developed electronic detection scheme. Most biological processes (electrostatic interaction and charge transfer) allow electronic detection. This biological process can be merging of biology and electronics. Because of the rich potential of biosensors [47] and bioelectronics [48], recent research has focused on the interactions between biomolecules and inorganic systems. The integration of biological processes and molecules with fabricated

structures also offers both electronic control and sensing of biological systems and bioelectronically-driven nanoassembly.

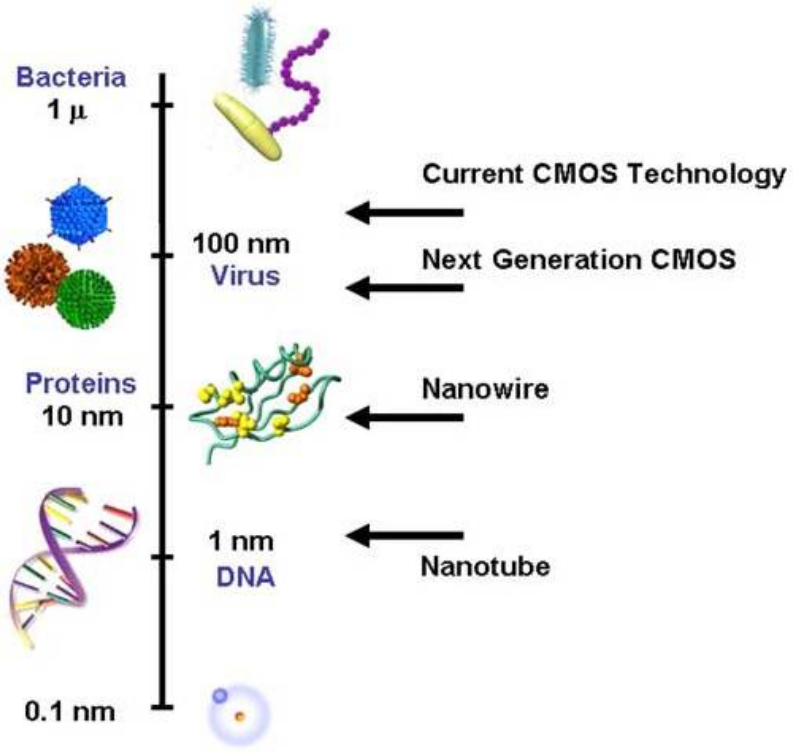

Figure 10. The dimensions of wires used in conventional CMOS technology, together with as-grown nanowires and carbon nanotubes. While the cross-section of nanofibers and inorganic nanowires is comparable to the size of typical proteins, single wall carbon nanotubes have a diameter comparable to DNA

Field effect transistors (FETs) with single carbon nanotube conducting channels and with nanotube network conducting channels have been fabricated and

their electronic characteristics examined. The devices respond to changes in the environment, effects have been examined using gas molecules with specific properties [49-54]. CNT based electronic device eventually integrate biology and electronics into a common platform suitable for electronic control and biological sensing as well as bio electronically driven assembly [55]. Carbon nanotubes have been functionalized to be biocompatible and to be capable of recognizing proteins [56–58]. Often this functionalization has involved noncovalent binding between a bifunctional molecule and a carbon nanotube in order to anchor a bioreceptor molecule with a high degree of control and specificity. The unique geometry of carbon nanotubes has also been used to modify carbon nanotube-protein binding. The conformational compatibility, driven both by steric and hydrophobic effects, between proteins and carbon nanotubes has been examined using streptavidin and other proteins. For example, streptavidin has been crystallized in a helical conformation around multi-walled carbon nanotubes [59]. The tendency of biological materials to self-organize has been used to direct the assembly of carbon nanotube structures [60].

Several different detection method can be employed for biomolecule sensing applications. The presence of an immobilized biomolecule, or the reaction between biomolecules can be followed by examining the change in the device characteristics after the interaction. The DC is measured in a conventional configuration applying the bottom gate. Fig. 11 shows the measurement scheme adapted bottom gate.

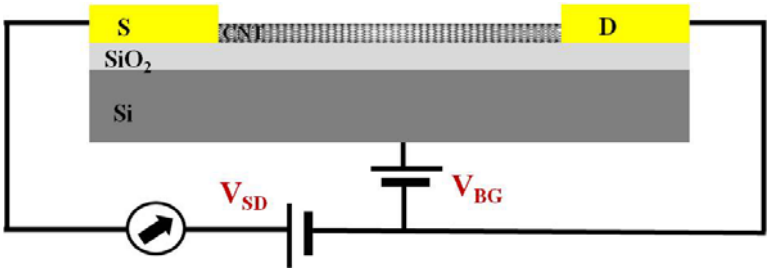

Figure 11. A Schematic of a single nanotube field effect transistor (FET) using bottom gate

Most of the biological interactions take place in an appropriate buffer environment. Real time signal acquisition and analysis may have significant impact on the biological sciences for several reasons. First, the time scales for biological processes may be measured directly. The time taken for a protein to undergo conformational changes or DNA duplex formation and its complement to form a duplex could be measured directly. Second, the electronic data may produce electronic signatures specific to a biological process. For example, if each binding of a different antigen to an antibody results in a particular electronic signature, then the different antigens may be distinguished from each other. This could dramatically alter the landscape of biological sensing, and aid the development of practical biosensors by solving the problems of poor cross-sensitivities. Biomolecules undergo a variety of fluctuations and conformational changes that span several orders of magnitude.

Pico-second time scales characterize intra molecular vibrations [61], with anharmonic relaxations [62] on the order of nano-seconds. Protein collapse occurs

at milli-seconds to seconds [63–69].

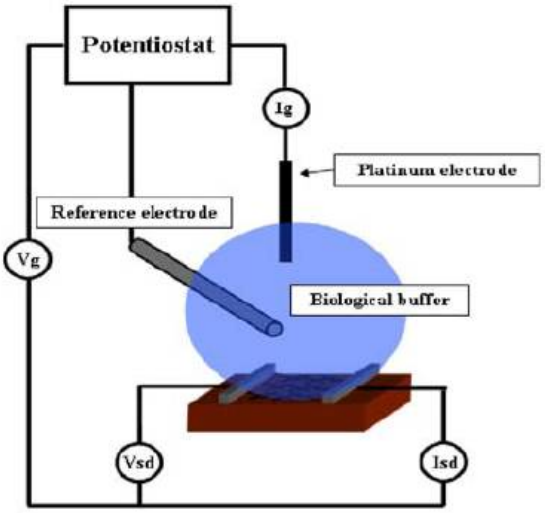

Figure 12. Schematic illustration of liquid gating. The gating is accomplished by immersing a Pt electrode in the conducting liquid that surrounds the network and the source and drain electrodes.

In the Fig. 12, an electrode is applied to the liquid and I_{SD} is measured as function of the voltage on the electrode. Electrochemical reaction occur at large gate voltages. These can be identified and avoided by monitoring the current between the gate and the conducting channel. The source and drain electrodes and all the conducting leads must be isolated from the buffer in order to avoid non-desirable reactions. A typical DC for both ‘‘liquid gating’’ and ‘‘bottom gating’’ is shown in Fig. 13 (a).

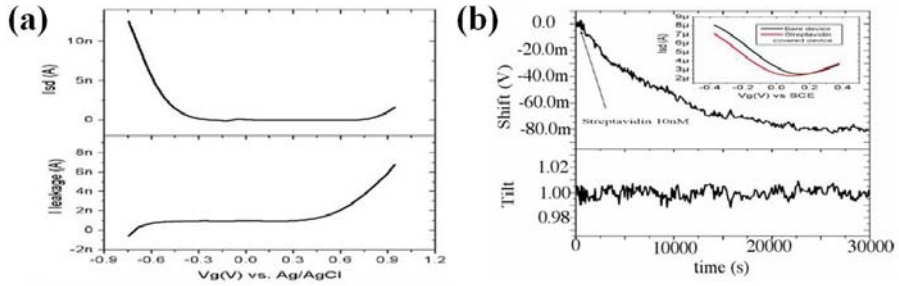

Figure 13. Real time monitoring for both liquid gate and bottom gate (a) Device characteristics (upper figure) and the so-called leakage current (measured between the Pt electrode and the S/D electrodes). The finite leakage current indicates the onset of electrochemical reactions. (b) Shift in the DC versus time during incubation with streptavidin. The slope (tilt) of the DC is not affected by the presence of streptavidin, indicating charge transfer between the biomolecule and the nanotube channel.

The two configurations result in a similar DC if an appropriate scaling of the x-axis is performed. This scaling is due to the different dielectric layers in the two cases: an oxide insulating layer for bottom gating and a hydration layer in the case of ‘‘liquid gating’’. In Fig. 13 (b), real time measurement of the change in the DC versus time allows real-time monitoring of the attachment of the protein to the device. Carbon nanotube based devices can use to monitor a variety of biologically-significant reactions. This is possible because most of these reactions involve local electric fields and charge rearrangement. Real time monitoring specific interactions between biomolecules is the most important objectives of biomolecule sensing [70–72].

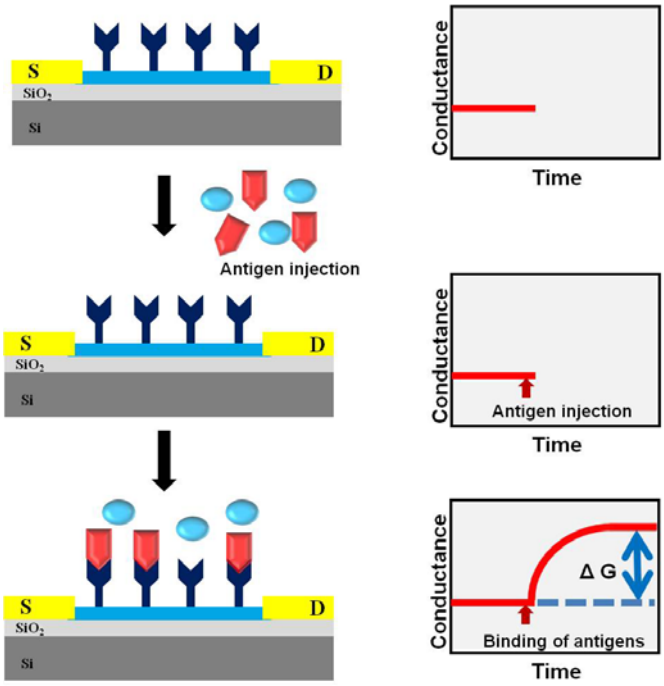

Figure 14. Carbon nanotube based biosensor detection principle of antibody-antigen specific binding. Left column: Schematic illustration show ab-ag binding process on the CNT-FET. Right column: CNT-FET electrical conductance change for ab/ag binding.

A carbon nanotube based biosensor detection principle that involves electronic detection is shown in Fig. 14. The next step in this direction is to examine device operation in a serum and to explore the sensitivity and specificity issues that arise in application areas such as early diagnosis applications.

1.2.3. Surface Plasmon Resonance (SPR) sensor

Surface Plasmon Resonance (SPR) sensors are extensively used as optical sensors for the detection of biological and chemical analytes. Due to this, SPR biosensors hold a great potential in fields such as food-safety, environmental protection and medicine [73]. SPR biosensors are also used in the analysis of biomolecular interactions. Hence SPR biosensors are also used in real-time monitoring of biomolecules binding to target molecules on the sensor.

A surface plasmon wave is an electromagnetic wave that propagates along the interface of metals and a dielectric. Metals such as gold, silver and copper exhibit negative real permittivity at optical wavelengths. However gold is the most widely used metal for SPR based sensor because of its chemical stability and abundant surface functionalization techniques [74].

The principle behind total internal reflection is that light incident at the interface between materials of refractive indices n1 and n2 (where n1 > n2) is completely reflected beyond a critical angle theta (θ). Surface plasmon resonance occurs when these two conditions are satisfied:

1. The incident angle must be greater than the critical angle
2. The component of incident light's that is parallel to sensor surface matches with the wave vector of surface plasmon wave.

When this happens, the energy of the incident photon is transferred to surface plasmon wave. Fig. 15 shows the prism coupler configuration for exciting

surface plasmon waves. The prism is used to couple some light to SP wave and reflect some light to an optical photo detector. Since an evanescent electric field extends away from the metal surface into the surrounding dielectric, changes in the optical properties of the dielectric will cause the resonance to shift to a different wavelength. Surface plasmon waves can also be excited by two other systems, grating-couplers and optical waveguides.

Concept of surface plasmon resonance biosensing: Surface plasmon waves are sensitive to changes in the refractive index of dielectric. This is the principle behind SPR biosensors - i.e. binding of a target analyte to immobilzed biomolecular recognition element produces a local increase in refractive index at the sensor surface.

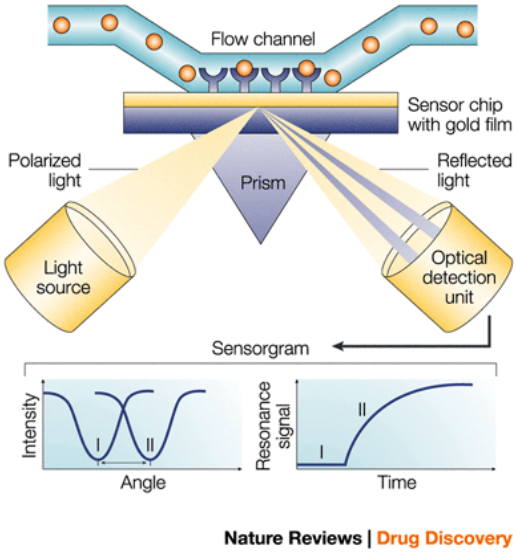

Figure 15. Typical set-up for a SPR biosensor

The operation of SPR sensor details demonstrated in Fig. 15. SPR detects changes in the refractive index in the immediate vicinity of the surface layer of a sensor chip. SPR is observed as a sharp shadow in the reflected light from the surface at an angle that is dependent on the mass of material at the surface. The SPR angle shifts (from I to II in the lower left-hand diagram) when biomolecules bind to the surface and change the mass of the surface layer. This change in resonant angle can be monitored non-invasively in real time as a plot of resonance signal (proportional to mass change) versus time. [75].

Chapter II

CNT-based biosensor for detection hepatitis B

2.1. CNT-FET biosensor

2.1.1. Fabrication of CNT-FET

The CNT biosensor was fabricated base on a field effect transistor (FET) structure, Fig. 16 depict the fabrication process of carbon nanotubes field effect transistor (CNT-FET). The single-wall carbon nanotubes (SWNTs) were grown by the patterned catalyst growth technique [76]. For catalysts, square patterns of 3 × 3 μm^2 were made using electron beam lithography and were deposited on silicon substrate with a 200 nm thick silicon oxide layer. Catalyst (Fe $(NO_3)_3 \cdot 9H_2O$, MoO_2 $(acac)_2$ and alumina nanoparticles) was dissolved in the ethanol solution and

dropped the catalyst solution on the patterned Si/SiO_2 substrate. After forming the catalyst pattern, substrate was soaked in the acetone for lift-off (Fig. 16). For thermal chemical vapor deposition (CVD) growth, the catalyst deposited substrate is heated in a furnace to reach 900 °C in an argon atmosphere. After argon flow, methane was flowed at a flow rate of 500 sccm. The methane flow is maintained for 5 min at 900 °C. Methane was used carbon source during growing the carbon nanotube. After methane flow, argon flowed until the furnace cools to room temperature.

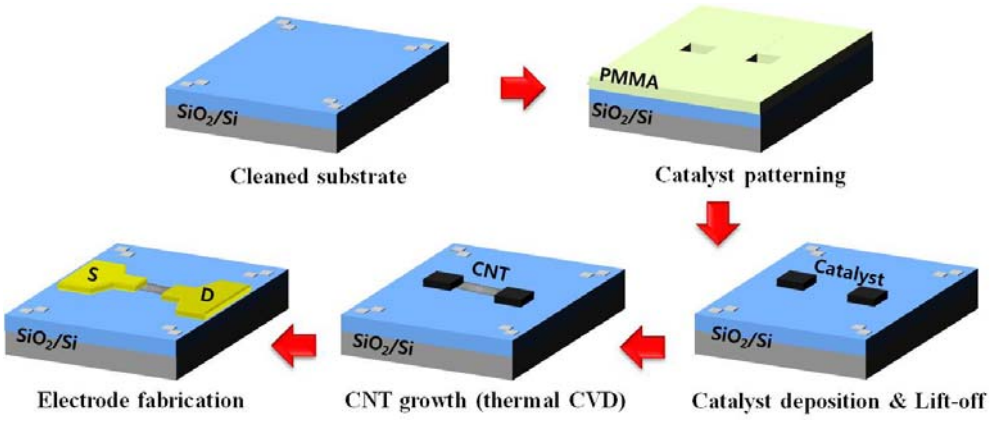

Figure 16. Schematic diagram of the carbon nanotube-field effect transistor (CNT-FET) fabrication process

Fig. 17 (a) shows the scanning electron beam microscope (SEM) of grown

carbon nanotube and Fe/Mo catalyst square. CNT was connected between the two catalyst pattern and straight line. Fig. 17 (b) is the atomic force microscope (AFM) image of as-grown CNT. By the AFM measurement, the diameter of CNT was about 1.5 nm. Source (S) and drain (D) electrical contacts to the CNT were made via electron beam lithography and thermal evaporation technique. Electrodes were made by depositing Cr/Au (5 nm /50 nm) and using a lift-off technique, followed by rapid thermal annealing (RTA) at 450 °C for 30 s in hydrogen circumstance to form ohmic contacts.

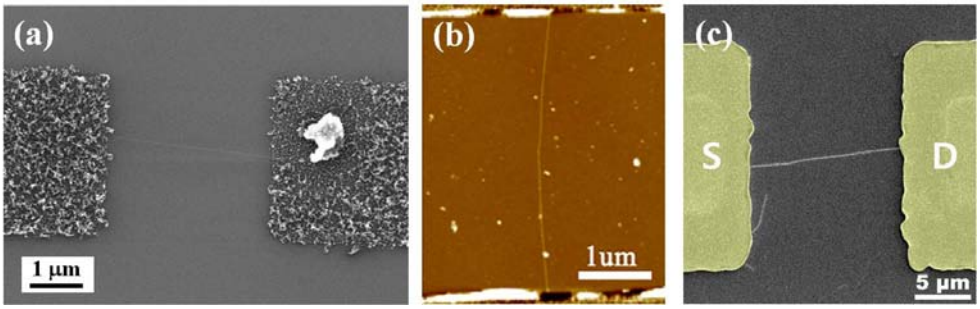

Figure 17. SEM image of the Carbon nanotube-field effect transistor(CNT-FET) (a) SEM image of after CNT growth using thermal CVD (b) AFM image of as-grown CNT (c) SEM image of after source and drain electrode fabrication

Fig. 17 (c) is the SEM image of CNT-FET after source and drain electrode definition. After electrodes definition, we measured electrical characteristics of the CNT-FET device. Fig. 18 (a) and (b) show the source-drain current (I_{DS})-voltage (V_{DS}) and the source-drain current (I_{DS})-gate voltage (V_{BG}) curves measured in the

ambient condition for the bare CNT-FET, where a heavily doped Si substrate was used as a bottom gate electrode. In the Fig 18 (a), the linear I_{DS}-V_{DS} curve confirms of ohmic contact. The CNT-FET bottom gate voltage dependence curve (Fig. 18 (b)) indicates fabricated CNT was a p-type semiconductor.

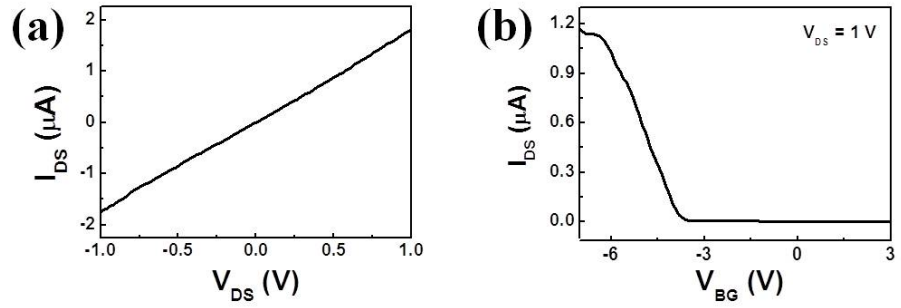

Figure 18. Electrical characteristics of single CNT-FET (a) The typical I_{DS}-V_{DS} curve of the CNT-FET device (b) The typical I_{DS}-V_{BG} curve measured at V_{DS} = 1 V

2.1.2. PDMS micro fluidic channel fabrication

Most biomolecules interaction occurs in an aqueous condition. So, we PDMS micro fluidic channel was mounted onto the CNT-FET biosensor. We injected and controlled the flow rate of solution the solution using syringe pump to assemble the biomolecules at the CNT surface [77, 78].

First, we fabricated the mold of micro fluidic channel using SU-8 & photo-lithography. SU-8 2150 resist (negative photo resist) was spin coated on the Si wafer (1st step 500 rpm for 10 sec with acceleration of 100rpm/sec, 2nd step 2000 rpm for 30 sec with acceleration of 300 rpm/sec.), prebaked at 65 °C for 7 min and at 95°C for 60 min. After prebaking step, followed UV (350nm) exposure for 90 s (exposure energy: 350~370 mJ/cm^2). After UV exposure, post-baking was conducted at 65°C for 10 min and at 95°C for 20 min. Develop times was 20 min in SU-8 developer, after develop washing with isopropyl alcohol & N_2 dry. After development process, the SU-8 pattern (channel) was formed with 250 μm thickness and 300 μm width (Fig. 19 (c)).

PDMS is the mixture of PDMS and curing agent (hardener) (10:1). The mixture of PDMS was poured onto the mold and the air bubble was extracted by vacuum pump. After eliminating the air bubble, PDMS was hardened at 80°C in an oven for 4 h (Fig.19 (d)). PDMS micro fluidic channel was attached with CNT-FET device as follows process. First, PDMS & toluene mixture (volume ratio 10:1) was spin-coated on the slide glass at 3000 rpm for 30 sec and baked at 70°C for 15 min then PDMS micro fluidic channel was positioned onto the slide glass. After 1 minute PDMS micro fluidic channel was detached from the slide glass and PDMS channel was attached to the device with well alignment, and then it was baked in oven (80°C) for 2 h.

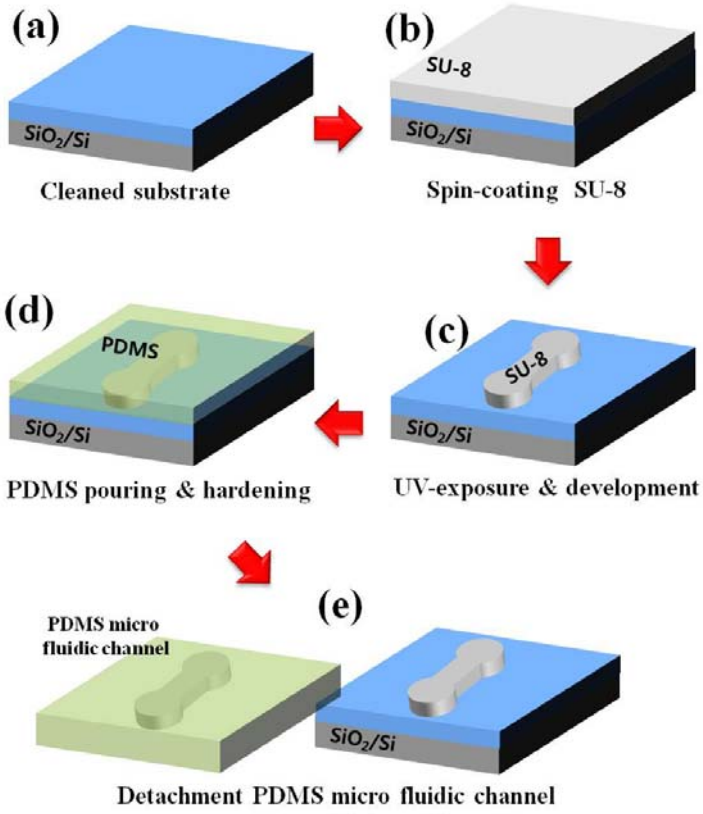

Figure 19. Schematic diagram of PDMS micro fluidic channel fabrication

2.1.3. Experimental process

The CNT-metal contacts were passivated using SiO_2 to minimize the contact effect. Before immobilizing hepatitis B antibody onto the CNT surface, the CNT was incubated in 1 *mM* pyrenebutyric acid N–hydroxylsuccinimide ester (chemical

linker) in methanol to introduce the amino-active succinimide ester, resulting in the binding of the pyrene residue to the sidewalls of the SWNT [79, 80]. Fig. 20 is depict the function of chemical linker.

Then, hepatitis B antibody was immobilized on the CNT surface by injecting 5 μg/ml antibody solution into the micro fluidic channel and leaving for 1 h. Before hepatitis B antigen injection, we injected phosphate buffered saline (PBS, pH 7.4) solution and measured electrical conductance.

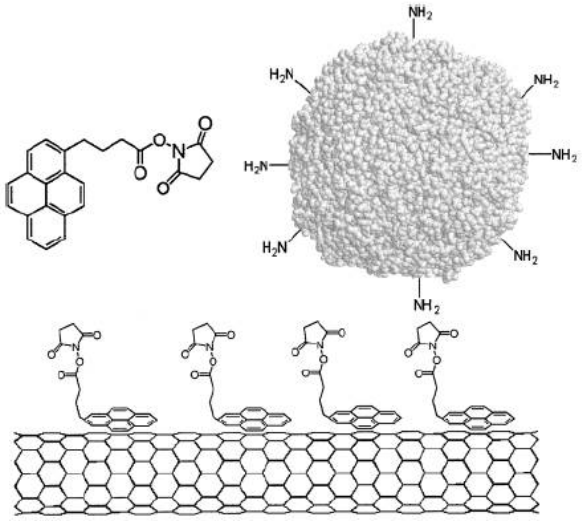

Figure 20. pyrenebutyric acid N–hydroxylsuccinimide ester irreversibly adsorbing onto the sidewall of a SWNT via π-Stacking. Amine groups on a protein react with the anchored succinimidyl ester [79].

After electrical conductance saturation, we introduced the hepatitis B antigen. The electrical conductance was measured as a function of time while hepatitis B

antigen was added into the micro fluidic channel. All chemical modification and binding events between antibodies and antigens occurred inside micro fluidic channels [81].

Fig. 21 shows the process of sensor preparation, linker assembly, protein assembly and real time measurement process.

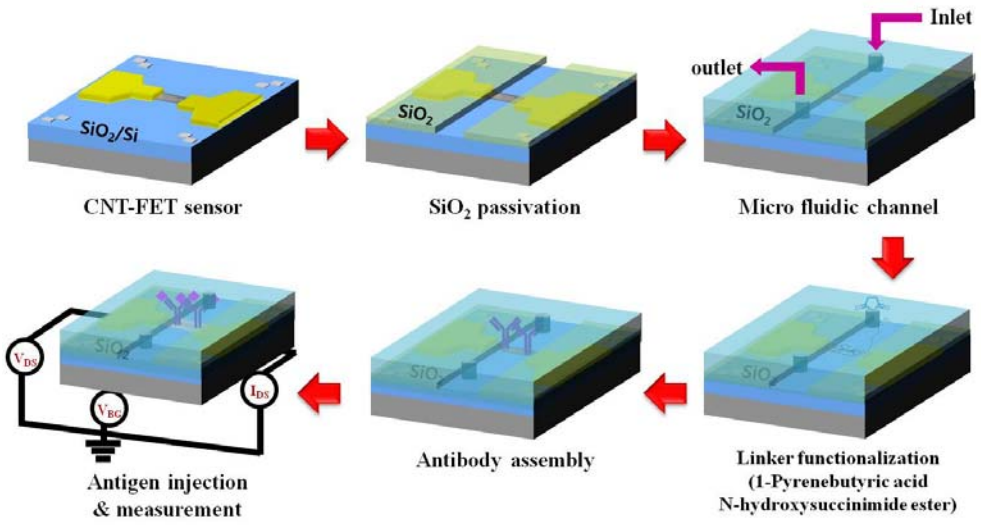

Figure 21. Schematic diagram of assemble and real time measurement process using CNT FET sensor.

2.2. Results and Discussion

2.2.1. Detection of Hepatitis B antibody-antigen binding

At first, to test the specificity of the CNT biosensor, we measured the conductance as a function of time while 1 μg/ml bovine serum albumin (BSA) solution was injected into the hepatitis B antibody assembled CNT-FET sensor. As shown in Fig. 22 (a), no current change was found, suggesting that BSA was not bound to hepatitis B antibody. Subsequently, 3 μg/ml hepatitis B antigen was injected into the micro fluidic channel and the conductance was observed to increase and then be nearly constant within 10 min. This result indicates that specific binding between hepatitis B antibody and antigen was successfully conducted at the CNT surface. Fig. 22 (b) shows the $I_{DS} - V_{BG}$ curves measured before and after adding hepatitis B antigen.

The introduction of hepatitis B antigen led to increase the current and shift the threshold voltage to the positive voltage [82, 83]. These results are consistent with the results shown in Fig. 22 (a).

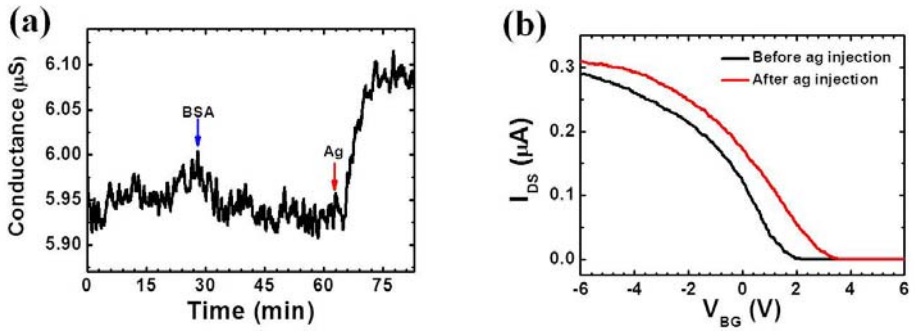

Figure 22. Electrical characteristics of CNT-FET sensor after hepatitis B antigen injection. (a) Real time detection of electrical conductance measured at V_{DS}= 0.5 V, V_{BG} = 0 V while BSA solution and 3μ*g/ml* of hepatitis B antigen was added. (b) I_{DS}-V_{BG} curves measured at V_{DS} = 1 V before and after adding hepatitis B antigen.

2.2.2. Real-time detection of hepatitis B antigen

We also investigated the concentration dependence of hepatitis B antigen on the conductance. As shown in Fig. 23 (a), the current increased with increasing the concentration of hepatitis B antigen. In Fig. 23 (b), the plot of the current versus the antigen concentration is presented. The current increased almost linearly to the concentration in the semi-logarithm scale. Compared with the ELISA method, a CNT biosensor has a several advantage. It can be used for real time monitoring application, label free detection and a very small sample volume is needed [84, 85].

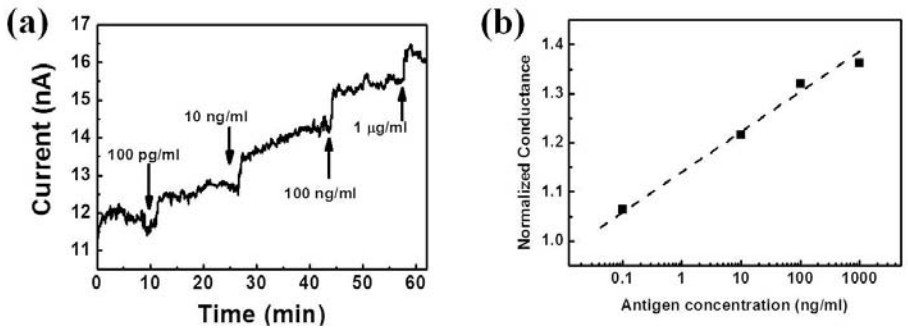

Figure 23. Hepatitis B ag concentration dependence of CNT-FET sensor. (a) Response to various concentrations of hepatitis B antigen. Arrows indicate when hepatitis B antigen was added. (b) The normalized conductance versus the concentration of hepatitis B antigen in semi-logarithm scale.

After electrical measurements of the hepatitis B antibody and antigen binding, the CNT channel was examined using an atomic force microscope (AFM) to confirm the binding of hepatitis B antigen to antibody. In order to see whether hepatitis B antigen was really bound to hepatitis B antibody immobilized on the CNT surface, the CNT biosensor was examined using the AFM after detecting hepatitis B antigen. As shown in Fig. 24 (a) and (b), the CNT biosensor used to detect hepatitis B antigen exhibited a higher height and a wider width than the bare CNT. This finding confirms that the measured conductance change was caused by binding between hepatitis B antibody and antigen.

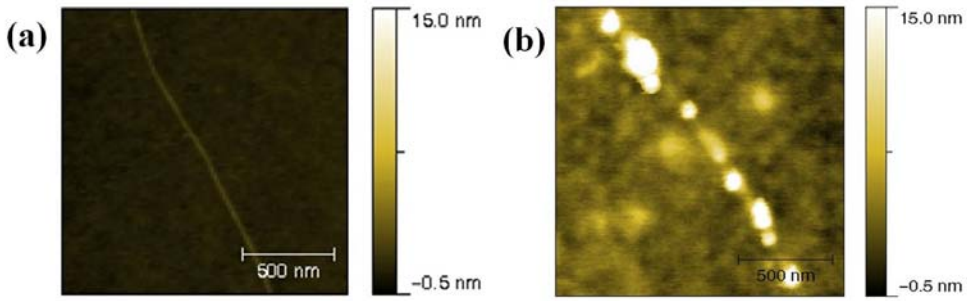

Figure 24. (a) AFM image of the bare CNT. (b) AFM image of the CNT after binding hepatitis B antibody and antigen.

Chapter III

Carbon Nanotube - based dual mode biosensor

3.1 Experimental details

3.1.1. What is dual-mode carbon nanotube sensor?

CNT-FET sensors are several problems to be solved for real applications, such as sensor-to-sensor variation, unspecific binding, etc. To overcome the above problems, we have proposed a dual mode biosensor that enables the detection of biological events by simultaneously measuring both changes in electrical conductance and surface plasmon resonance (SPR).

Fig. 25 is the dual mode biosensor has the structure of a CNT metal semiconductor field effect transistor (CNT-MESFET). We fabricated CNT-MESFET sensor using long CNT, transparent quartz and $SiSiO_2$ substrate.

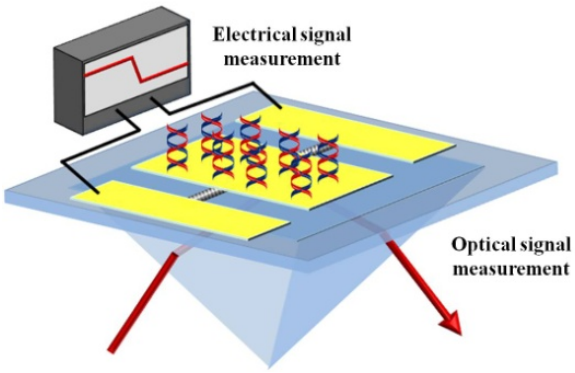

Figure 25. Schematic diagram of a dual mode CNT-MESFET biosensor. Dual mode biosensor is composed of electrical and optical measurement parts.

The Schottky barrier forms at an interface between the Au strip and the CNT; thus, the Au strip plays the role of a top gate. As a result, charged biomolecules, which bind to receptors immobilized on the surface of the Au strip, may be detected by measuring the change in the electrical conductance of the CNT. In addition, the transparent substrate allows the CNT-MESFET to detect SPR occurring at the interface between the Au top gate and the transparent substrate when an incident beam of polarized light of a given wavelength is directed onto the surface at a given angle through a prism (Fig. 25). Biological events can be detected and quantified by measuring the changes in SPR.

Compared with CNT-FET biosensors, SPR sensors provide better reliability, although their sensitivity is relatively low [86, 87]. On the other hand, the CNT-FET biosensors offer ultra-high sensitivity, although their performances are dependent on the sensor. For the dual mode biosensor, SPR and conductance measurements may complement each other, so that both high sensitivity and reliability may be obtained together. Furthermore, the chemical modification of the Au surface utilized in the SPR biosensors is well known, so unspecific binding would be more easily inhibited in the dual mode biosensor compared to the CNT-FET biosensors. In this paper, we have fabricated dual mode biosensors on quartz substrates and we demonstrated that DNA hybridization can be detected by measuring the change in electrical conductance and SPR at the same time.

3.1.2. Fabrication of CNT-MESFET

We fabricated the CNT-MESFETs on SiO_2/Si substrates to test the electrical characteristics of them. CNT-MESFET device fabrication process was noted in Fig. 26. First, we fabricated Single-walled CNTs (SWNTs) FET device as described at the chapter 2.1.1.

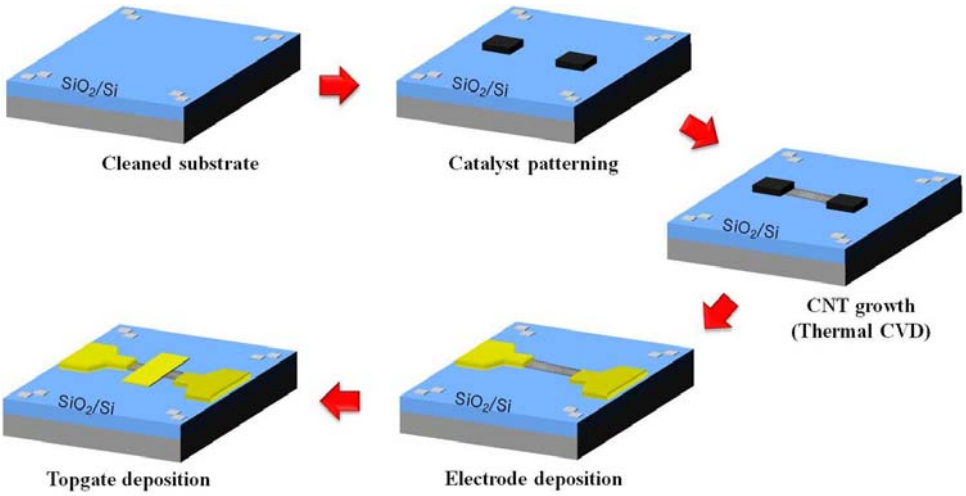

Figure 26. Schematic diagram of CNT-MESFET fabrication

To determine whether the CNT connected between source and drain electrodes was metallic or semiconducting, the source-drain current (I_{SD}) was measured as a function of the bottom gate voltage (V_{BG}) for all devices. The heavily doped Si substrate was used as the bottom gate and electrical measurements were carried out using a semiconductor parameter analyzer. The top gate was fabricated by electron lithography and thermal deposition (Cr/Au (2 nm / 25 nm)) and lift-off technique. Top gate was defined only on the middle of the semiconducting CNT, as shown in Fig. 27 (b).

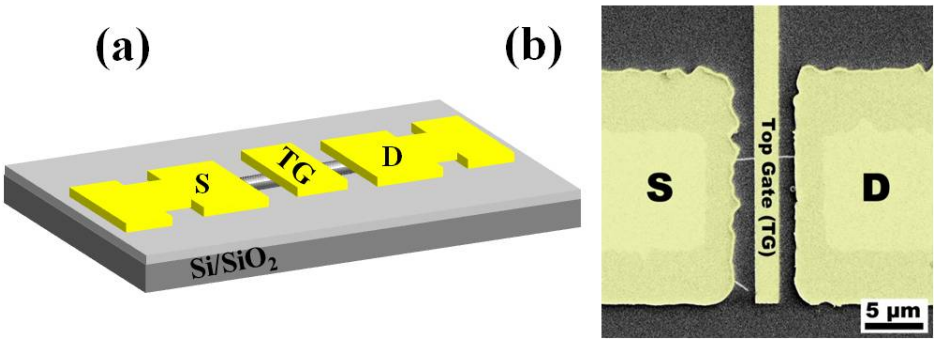

Figure 27. (a) A schematic diagram of a CNT-MESFET device. (b) SEM image of a CNT-MESFET on Si/SiO_2 substrate.

3.1.3. Electrical characteristics of CNT-MESFET

We characterized the electrical properties using three electrodes, source (S), drain (D), and top gate (TG) electrodes, *I–V* curves were measured under ambient conditions (Fig. 28 (a)). The I_{SD}-V_{SD} curve measured between the source and drain electrodes was linear, whereas the I_{STG} - V_{STG} and I_{DTG} - V_{DTG} curves exhibited diode-like behaviors, where I_{STG} (or I_{DTG}) stands for the current measured between the source (or drain) and top gate electrodes. These results suggest that the Schottky contacts formed between the top gate electrode and the CNT, while ohmic contacts formed between the source-drain electrodes and the CNT owing to the heat treatments.

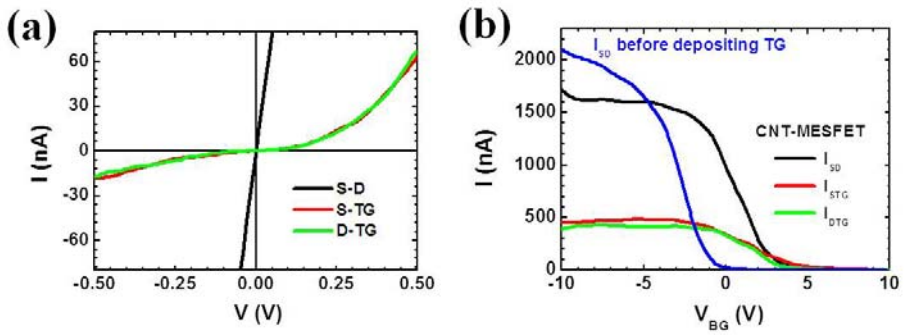

Figure 28. Electrical characteristics of CNT-MESFET (a) *I-V* curves measured using source (S), drain (D), and top gate electrodes (TG). (b) I-V_{BG} curves measured at V=1 V. I_{SD} is the current measured between the source and drain electrodes, I_{STG} is the current measured between the source and top gate electrodes, and I_{DTG} is the current measured between the drain and top gate electrodes.

Fig. 28 (b) shows the I_{SD}-V_{BG}, I_{STG}-V_{BG}, and I_{DTG}–V_{BG} transfer curves measured at V=1 V. As expected from the measured *I-V* curves in Fig. 20 (a), I_{STG} and I_{DTG} were lower than I_{SD}. However, all curves exhibited p-type semiconducting behaviors with nearly identical threshold voltages, V_{th}, although V_{th} was found at the higher V_{BG} compared to the I_{SD}-V_{BG} curve measured before depositing the top gate. From these results, we concluded that the semiconducting properties of the CNT were not significantly affected by depositing the top gate.

Most biological interactions occur under aqueous conditions, so biosensors usually operate in an aqueous environment. To investigate the effects of a liquid gate voltage (V_{LG}) on the electrical properties of the CNT-MESFET, we passivated

the source-drain electrodes and the CNT regions uncovered by the top gate by depositing a SiO_2 thin film, leaving only the Au top gate exposed to the solution, and then mounted a polydimethylsiloxane (PDMS) well over the CNT-MESFET (Fig. 29).

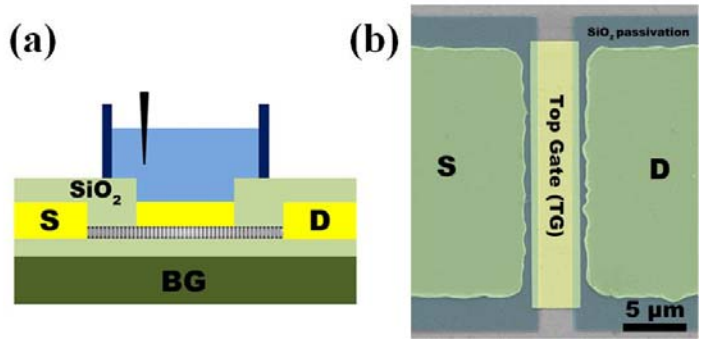

Figure 29. (a) A schematic diagram of a CNT-MESFET with a PDMS well. (b) SEM image of a CNT-MESFET passivated by depositing a SiO_2 thin film

Subsequently, we filled the PDMS well with a 10 mM solution of the phosphate buffered saline (PBS, pH 7.4) and inserted an Ag/AgCl reference electrode used as the liquid gate (LG). Fig. 30 depicts the I_{SD}-V_{LG} curve measured at V_{SD}=10 mV and the leakage current (I_{SLG}) between the source and the liquid gate. The p-type semiconducting behaviors were clearly observed with negligible I_{SLG}. This result indicated that I_{SD} of the CNT-MESFET could be modulated by applying V_{LG} in spite of the shielding effect from the Au top gate.

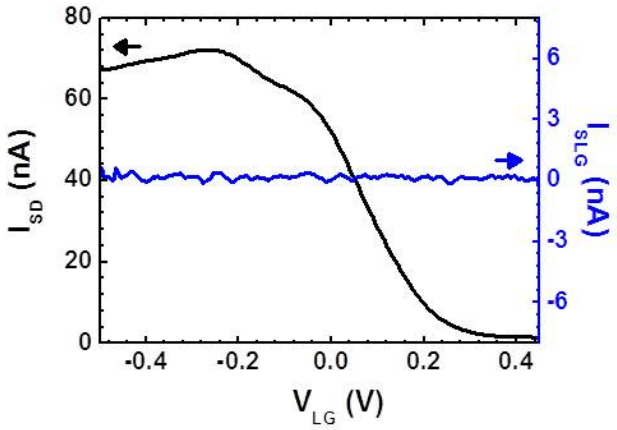

Figure 30. I_{SD}-V_{LG} and I_{SLG}-V_{LG} curves measured at V_{SD}=10 mV for the CNT-MESFET.

For comparison, we also measured the I_{SD} - V_{LG} curve at V_{SD} = 10 mV for the CNT-FET without the top gate (Fig. 31). A clear difference was seen in a subthreshold swing defined as $S = dV_{LG}/d(\log I_{SD})$ [88]. The values of S were estimated to be approximately 0.1 and 0.23 V/decade for the CNT-MESFET and the CNT-FET, respectively, which were smaller than $S \approx 1.7$ V/decade estimated from the I_{SD}-V_{BG} curves for both devices (Fig. 28 (b)). These findings implied that the CNT-MESFET and CNT-FET had different values of liquid gate capacitance, whereas their bottom gate capacitance was nearly identical.

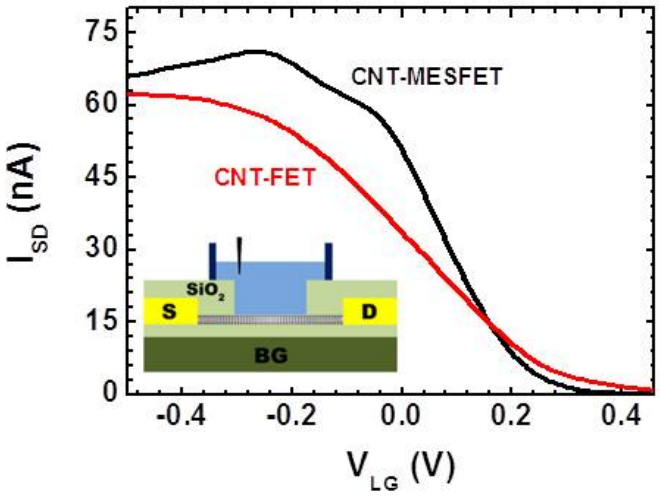

Figure 31. I_{SD}-V_{LG} curves measured at V_{SD}=10 mV for the CNT-FET and CNT-MESFET. The inset shows a schematic diagram of the CNT-FET with the PDMS well. The inset shows a schematic diagram of the CNT-FET with the PDMS well.

In the case of the liquid gate, the gate capacitance was approximately given by the double layer capacitance, $C_{dl} = \varepsilon A/x_{OHP}$, where ε is the dielectric constant of the electrolyte, A is the area of the surface exposed to the electrolyte, and x_{OHP} is the distance to the outer Helmholtz plane [89, 90]. Since the CNT-MESFET might have a larger A than the CNT-FET, the steeper transition of I_{SD} or the smaller S observed for the CNT-MESFET may possibly be ascribed to the larger liquid gate capacitance of the CNT-MESFET.

In order to more clarify the effects of gate capacitance on the I_{SD}-V_{LG} transfer curves, we also fabricated a CNT-MOSFET (metal oxide semiconductor field

effect transistor) with a 50 nm-thick Al_2O_3 dielectric between the CNT channel and the Au top gate (inset of Fig. 33 (a)). Fig. 33 (a) shows the I_{SD}-V_{LG} curve of the CNT-MOSFET measured at V_{SD}=10 mV using the Ag/AgCl reference electrode.

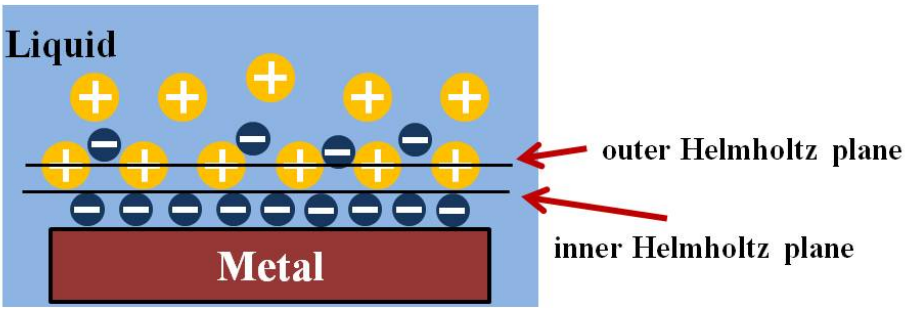

Figure 32. Schematic illustration of electrical double layer. The first layer of absorbed ions is referred to as the inner Helmholtz plane. Next is a layer of non-specifically absorbed, hydrated counter ions which represent an outer Helmholtz plane.

As V_{LG} increased, I_{SD} of the CNT-MOSFET decreased more slowly than I_{SD} of the CNT-MESFET or the CNT-FET. The plot of dI_{SD}/dV_{LG} versus V_{LG} for three devices, CNT-MESFET, CNT-FET, and CNT-MOSFET, showed clear differences (Fig. 33 (b)).

Since the liquid gate capacitance of the CNT-MOSFET was smaller than that of the CNT-MESFET or the CNT-FET due to the capacitance of the Al_2O_3 dielectric layer connected in series, this result supported the idea that the larger gate capacitance induced a more rapid decrease of I_{SD} with increasing V_{LG}.

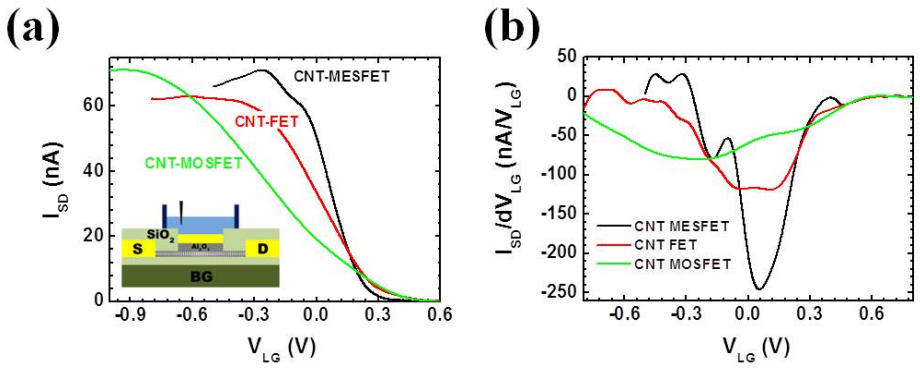

Figure 33. Liquid gate voltage dependence of CNT devices (a) I_{SD}-V_{LG} curves measured at V_{SD}=10 mV for the CNT-MOSFET, CNT-FET, and CNT-MESFET. The inset shows a schematic diagram of the CNT-MOSFET with the PDMS well. (b) dI_{SD}/dV_{LG} - V_{LG} curves for CNT-MESFET, CNT-FET, and CNT-MOSFET.

We thus obtained dual gates, the liquid and bottom gates, so we measured the I_{SD}-V_{BG} curves at V_{SD} = 0.1 V for different V_{LG}. As shown in Fig. 34 (a), the I_{SD}-V_{BG} curves of the CNT-MESFET were significantly altered by applying V_{LG}. As V_{LG} increased, I_{SD} at V_{BG}= 0 V was reduced and V_{th} was shifted to the lower V_{BG}. We also carried out similar measurements for the CNT-FET (Fig. 34 (b)). As in the CNT-MESFET, V_{th} was shifted to the lower V_{BG} with increasing V_{LG}. However, compared with the I_{SD}-V_{BG} curve of the CNT-MESFET, the I_{SD}-V_{BG} curve of the CNT-FET was less effectively modulated by V_{LG}, which was in accordance with results in Fig. 33.

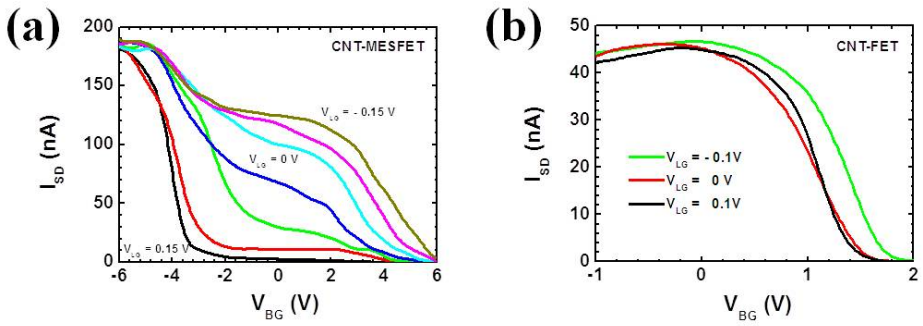

Figure 34. Dual gate voltage dependence of CNT-FET and CNT-MESFET (a) I_{SD}-V_{BG} curves of the CNT-MESFET measured at V_{SD}=0.1 V for different liquid gate voltages (V_{LG} = 0.15, 0.1, 0.05, 0, -0.05, -0.1, and -0.15 V). (b) I_{SD}-V_{BG} curves of the CNT-FET measured at V_{SD}=10 mV for different liquid gate voltages (V_{LG} = 0.1, 0, -0.1 V).

3.2. Experimental details

3.2.1. MMP-9 antigen detection

To detect MMP-9 using the CNT-FET biosensor, anti-MMP-9 was immobilized on the surface of CNTs using 1-pyrenebutanoic acid succinimidyl ester (Aldrich) as a linking molecule. A 1 *mM* solution of 1-pyrenebutanoic acid succinimidyl ester in methanol was introduced into the PDMS channel and left for 1 h. After washing with methanol, 1 μg/ml anti-MMP-9 solution was injected into the micro fluidic channel and left for 2 h to allow immobilization. To activate anti-MMP-9, the CNT-FET was incubated for 20 min at 37 °C in a mixture of 10 μl MMP-9 monomer, 70 μl activation buffer (50 mM Tris-HCl, pH 7.5, 150 mM NaCl, 5 mM $CaCl_2$), and 20 μl trypsin (0.5 mg TPCK-trypsin/1 ml activation buffer), and then trypsin was inhibited by adding a 10 μl aprotinin solution. Thereafter, the MMP-9 solution was added into the micro fludic channel and I_{SD} of the CNT-FET was measured in real time while MMP-9 was interacting with anti-MMP-9 immobilized on the CNT surface. For CNT-MESFET biosensor, cyc3-protein G, which is genetically engineered to contain three cysteine residues at the N-terminus, was used as a linker to immobilize anti-MMP-9 on the surface of Au

top gate. A 20 μg /ml cys3-protein G solution was flowed into the micro fluidic channel and left for about 30 minutes. Then, 1 μg/ml anti-MMP-9 solution was injected into the micro fluidic channel and left for 2 hours to allow immobilization. Next, anti-MMP-9 was activated as described above and I_{SD} of the CNT-MESFET was recorded in real time during addition of MMP-9.

3.2.2. DNA hybridization detection

To monitor DNA hybridization in real time, the CNT-MESFET was covered with a PDMS micro fluidic channel instead of the PDMS well (Fig. 35).

Then, probe single stranded DNA (ssDNA) molecules with thiol groups at one end were immobilized on the surface of the Au top gate. Immobilization was achieved via Au-S bonds by introducing a 1 μM solution of 30-mer probe ssDNA molecules (5′-SH-AAGTCAGTTATACGCGTCTAGTACCGTTTG-3′, purchased from M. Biotech Inc.) in PBS into the micro fluidic channel. Following immobilization, the CNT-MESFET was washed thoroughly by flowing PBS into the channel to remove the excess probe DNA. For hybridization experiments, a solution of 30-mer target ssDNA (5’CAAACGGTACTAGACGCGTATAACTGA CTT-3’), which was completely complementary to the probe ssDNA, was added

into the micro fluidic channel. While solutions of complementary target ssDNA molecules with different concentrations were flowed into the micro fluidic channel, source and drain current of the CNT-MESFET was recorded as a function of time.

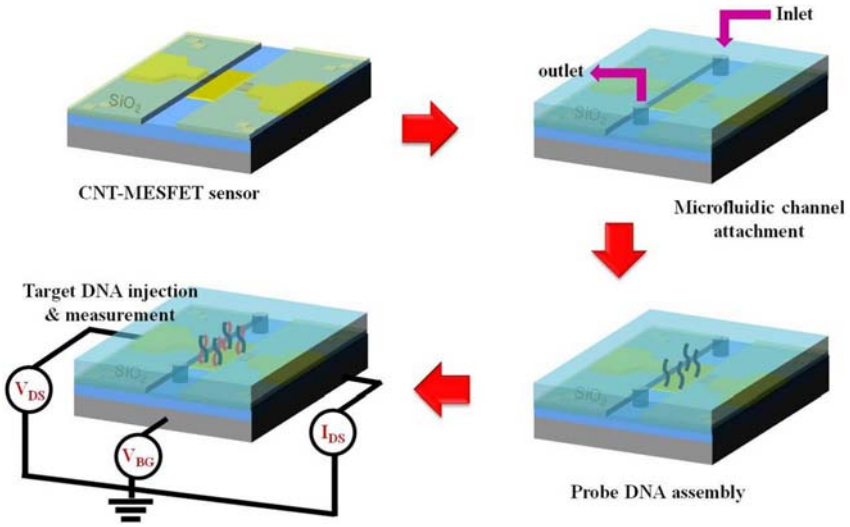

Figure 35. Schematic diagram of DNA assembly and measurement using CNT-MESFET sensor

3.3. Results and Discussion

3.3.1. Electrical signal measurement of DNA hybridization

While solutions of complementary target ssDNA molecules with different concentrations were flowed into the micro fluidic channel, I_{SD} of the CNT-MESFET was recorded at V_{BG} = 0 V as a function of time (Fig. 36).

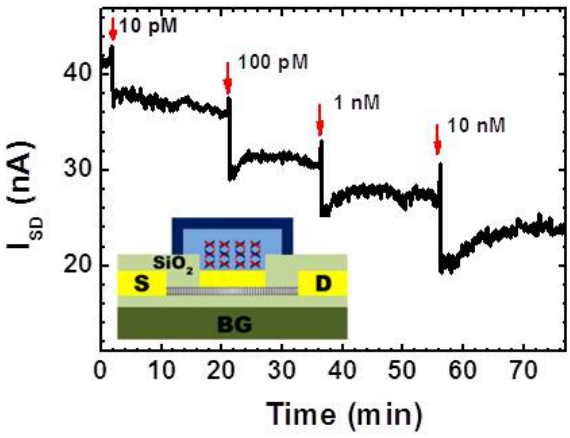

Figure 36. Real time monitoring of I_{SD} at V_{SD}=0.1 V during DNA hybridization in PBS. Arrows indicate the injection time of target ssDNA solutions with different concentrations. The inset shows the schematic diagram of the CNT-MESFET covered with a PDMS micro fluidic channel.

As reported for the CNT-FET biosensors [91, 92], I_{SD} decreased after DNA hybridization and further decreased with increasing concentrations of target ssDNA. To investigate the origin of decreased conductance, the I_{SD}-V_{LG} and I_{SD}-V_{BG} curves were measured before and after DNA hybridization, as shown in Fig. 37.

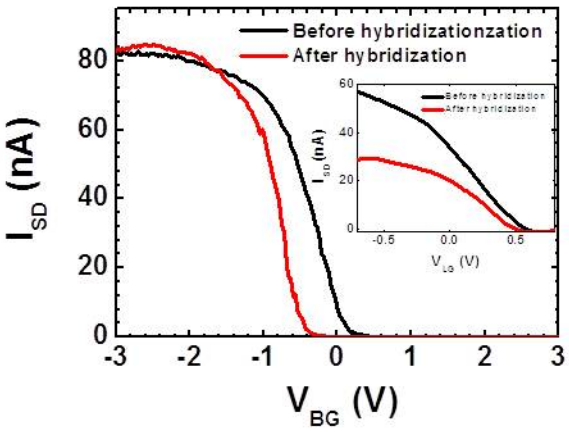

Figure 37. I_{SD}–V_{BG} curves of CNT-MESFET biosensor measured after DNA immobilization and hybridization. The inset shows the I_{SD}-V_{LG} curves measured at V_{SD}=50 mV before and after DNA hybridization.

DNA hybridization led to the shift in V_{th} to the lower V_{BG} or V_{LG} and the decrease in I_{SD} at V_{BG} or V_{LG}= 0 V. The decrease in I_{SD} may possibly be understood in terms of the energy band diagrams shown in Fig. 38.

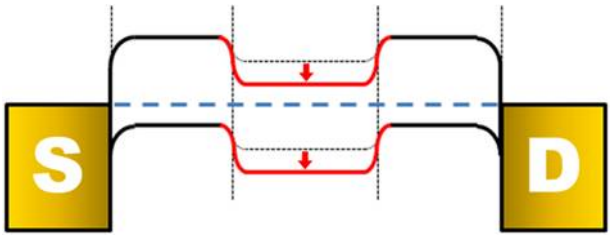

Figure 38. Energy band diagrams for the CNT-MESFET after DNA immobilization (dashed curve) and hybridization (solid curve)

DNA hybridization occurring on the Au surface is known to decrease the effective work function of Au [93, 94]. After hybridization, the potential of the CNT channel covered with the Au top gate is lowered, while the potential of the uncovered CNT portion is unchanged. As a result, we can imagine the band diagram of Fig. 38; the hybridization-induced depletion (as indicated by the arrows) draws a large channel resistance, causing the decrease in I_{SD} and the shift in V_{th}.

When we plotted the measured conductance normalized by the conductance before hybridization (G/G_o) as a function of the target ssDNA concentration (Fig. 39 (a)), we observed a linear relationship between G/G_o and the logarithm of target ssDNA concentration. For comparison, we also have displayed the data reported for the CNT network FET [92] in Fig. 39 (a). The CNT-MESFET exhibited a higher sensitivity and a wider detection range as compared to the CNT network FET. In addition to DNA hybridization, we also detected matrix metallopeptidase-9 (MMP-9) using both CNT-MESFET and CNT-FET, and compared their sensitivity, where anti-MMP-9 were used as a receptor of MMP-9 (Fig. 39 (b)).

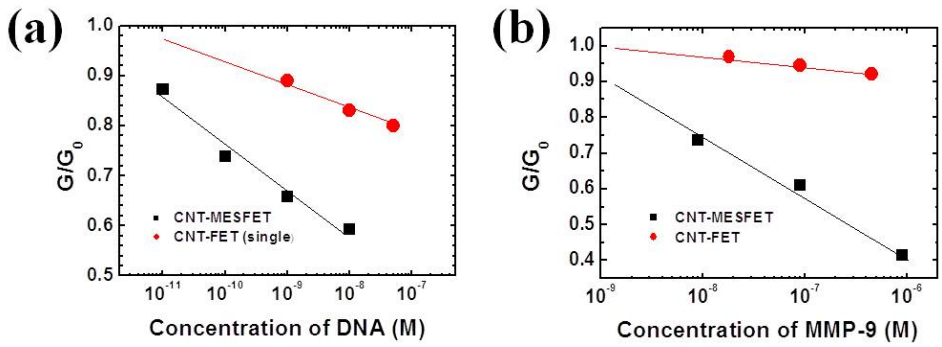

Figure 39. Normalized conductance of DNA hybrization and MMP-9 (a) G/G_o versus the concentration of target ssDNA molecules for the CNT-MESFET (rectangular symbols) and CNT- FET (circular symbols). (b) G/G_o versus the concentration of MMP-9 for the CNT-MESFET and CNT- FET.

As in DNA hybridization, I_{SD} decreased upon the binding of MMP-9 to anti-MMP-9 immobilized on the top gate or on the CNT surface. Fig. 39 (b) shows the plots of G/G_o versus the logarithm of MMP-9 concentration measured for CNT-MESFET and CNT-FET. The CNT-MESFET exhibited a steeper slope, supporting that the CNT-MESFET biosensor offers higher sensitivity than the CNT-FET. This higher sensitivity was probably attributed to the band bending in the bulk CNT, as illustrated in Fig. 38.

To determine whether it is possible to discriminate between hybridization with complementary and one-base mismatch DNA using the CNT-MESFET, we measured the conductance as a function of time while one-base mismatch DNA (5′- CAAACGGTACGAGACGCGTATAACTGACTT-3′) was added.

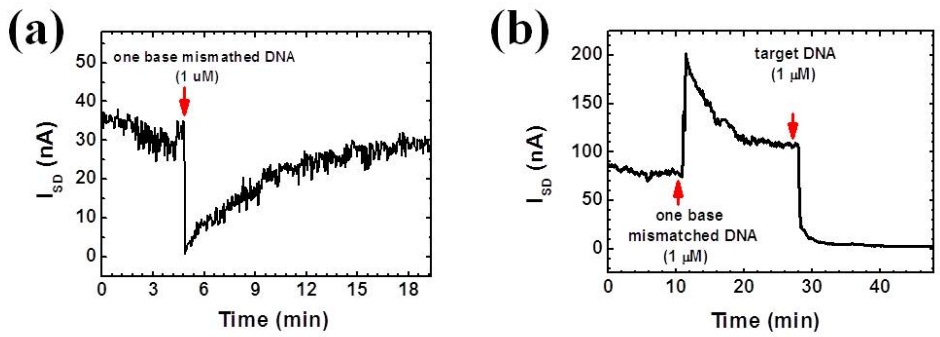

Figure 40. Single nucleotide polymorphism measurement using CNT-MESFET sensor (a) Real time monitoring of I_{SD} at V_{SD}=0.1 V while a 1 μM solution of one-base mismatch DNA solution was added and then followed by introduction of a 1 μM solution of complementary DNA solution. (b) Real time monitoring of I_{SD} at V_{SD}=0.1 V while a 1 μM solution of one-base mismatch DNA solution was added and then followed by introduction of a 1 μM solution of complementary DNA solution.

Unlike the completely complementary target ssDNA, the addition of one-mismatch DNA did not lead to the decrease in I_{SD}. Depending on the sensor, I_{SD} was restored nearly to the initial value (Fig. 40 (a)) or slightly increased (Fig. 40 (b)). However, the subsequent introduction of complementary DNA molecules resulted in the decrease in I_{SD} (Fig. 40 (b)), demonstrating that DNA hybridization could be detected even with single nucleotide polymorphism sensitivity.

3.3.2. Dual-mode measurement of DNA hybridization

The CNT-MESFET was fabricated on the quartz substrate for a dual mode biosensor (Fig. 33). Since the large top gate was necessary for SPR measurements, ultra-long SWNTs (> 18 mm) were grown on the quartz substrate by thermal CVD. Briefly, 10 mM of $FeCl_3$ solution was deposited on the edge of quartz substrate by micro-contact printing or dipping. The quartz substrate was placed in the middle of a 1 inch quartz tube and gradually heated to 950 ^oC in an argon/hydrogen gas atmosphere (200 sccm/60 sccm), followed by leaving at 950 ^oC for 10 min to form Fe nanoparticles. Then, a flow of methane (100 sccm) and hydrogen gas (60 sccm) at 950 ^oC for 1 h led to the growth of ultra-long SWNTs [95-97]. For electrical measurements, Au/Cr electrodes were prepared and rapid thermal annealing was performed at 450 ^oC for 30 s under vacuum. Subsequently, the Au top gate of 2 x 21 mm^2 was fabricated in the middle of the CNTs by photolithography and lift-off techniques.

Figure 41. SEM image of the CNT-MESFET fabricated on the quartz substrate.

The $I_{SD} - V_{SD}$ curves measured after DNA immobilization and hybridization are shown in Fig. 42 (a). As expected from the data in Fig. 36, the conductance was reduced by immobilization of target ssDNA molecules on the surface of the top gate even though several CNTs were connected between the source and drain electrodes.

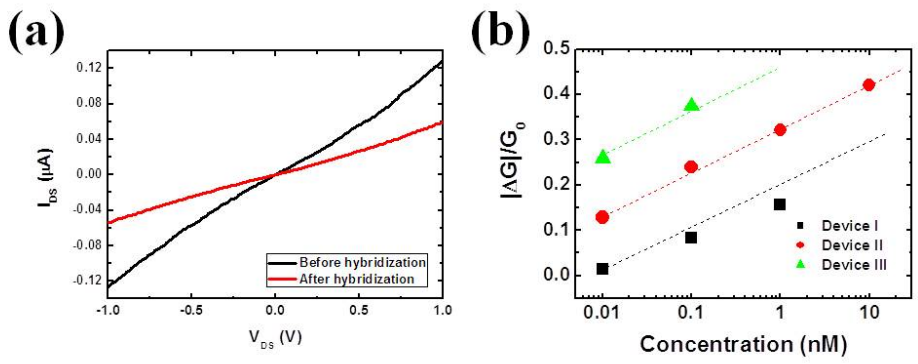

Figure 42. *I-V* curve change and normalized conductance of the CNT-MESFET sensor (a) I_{SD}-V_{SD} curves measured for the CNT-MESFET on the quartz substrate as-prepared, after DNA immobilization and hybridization. (b) $|\Delta G|/G_0$ versus the concentration of target ssDNA solution for three different CNT-MESFETs on SiO_2/Si substrates.

Fig. 41 (b) depicts the plots of G/G_o versus the logarithm of target ssDNA concentration obtained from three different CNT-MESFETs on Si/SiO_2i substrates. For three different sensors, we observed nearly parallel lines, although their intercepts were different. These findings suggest that sensor-to-sensor variation

might be calibrated if a complementary property, independent of the sensor, is measured concurrently, and the sensor-dependent intercept can be determined.

We therefore measured SPR characteristics using a custom optical set-up based on an angle-scanning scheme and implemented with dual concentric motorized rotation stages (URS75PP, Newport, Irvine, CA). Light from a He-Ne laser (36 mW, λ = 632.8 nm, Melles-Griot, Carlsbad, CA) is TM polarized and intensity-modulated by an optical chopper. The light is then incident through an SF10 prism substrate on the sample surface that is index-matched to the prism. The reflected light is detected by a photodiode (818-UV, Newport, Irvine, CA). The angular resolution of the rotation stage is 0.0002° (nominal). The measured signal is taken by a low noise lock-in amplifier (Model SR830, Stanford Research Systems, Sunnyvale, CA). The detection procedure is automated by LabView™ (National Instruments, Austin, TX).

The SPR curves, which were simultaneously measured with the I_{SD}-V_{SD} curves are presented in Fig. 43 (a). Immobilization of probe ssDNA molecules on the Au top gate led to an angle displacement of 0.12° in SPR reflectance minimum. After DNA hybridization caused by the addition of a 1 μM solution of target ssDNA molecules, the SPR angle was further shifted by 0.10°, although the SPR angle was unchanged by adding a 1 μM solution of non-complementary ssDNA molecules. These results are similar to the results reported by others [87, 98].

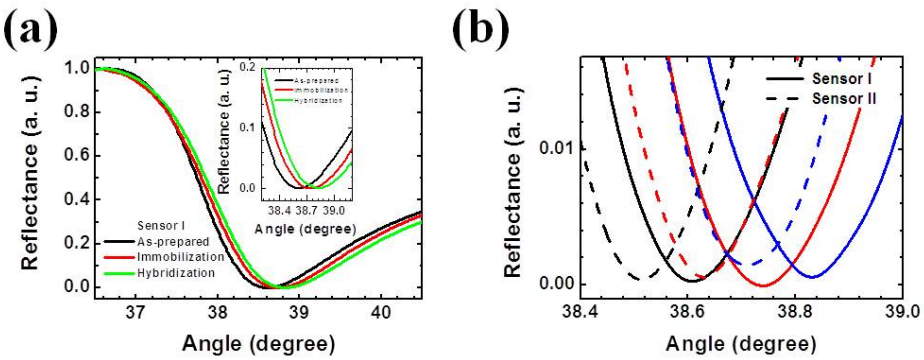

Figure 43. SPR signal of the CNT-MESFET on the quartz substrate (a) SPR curves measured for the CNT-MESFET on the quartz substrate as-prepared, after DNA immobilization and hybridization. The inset is an expanded view of SPR minima. (b) SPR curves measured for two different CNT-MESFETs on the quartz substrate as-prepared (black curves), after DNA immobilization (red curves) and hybridization (blue curves).

To evaluate whether different sensors yield the same displacement of SPR angle for a given concentration, we measured the SPR curves for another sensor prepared similarly (Fig. 43 (b)). After a 1 μM solution of target ssDNA molecules was added to induce DNA hybridization, the SPR angle was shifted by approximately 0.10°, indicating that the SPR measurements provided reproducible data independently of the sensor.

Fig. 44 displays the real-time response of conductance and SPR reflectance measured simultaneously while the DNA molecules were hybridized. From these simultaneously measured conductance and SPR reflectance, the value of the

sensor-dependent intercept (Fig. 43 (b)) is possibly estimated, which is necessary to calibrate the sensor-to-sensor variation.

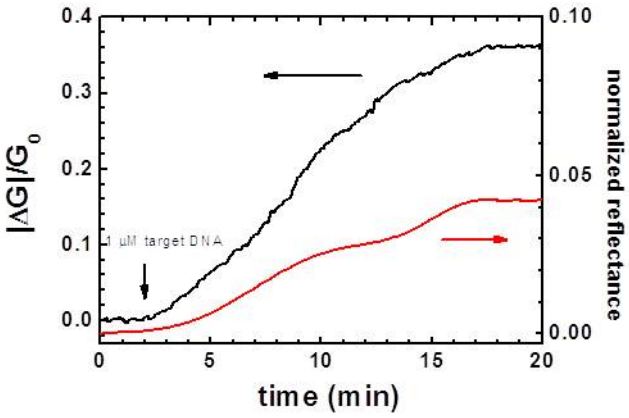

Figure 44. Real-time response of $|\Delta G|/G0$ and normalized reflectance simultaneously measured during DNA hybridization. The SPR reflectance was measured at 38°.

Chapter IV

CNT-MESFET biosensor using CNT thin film

4.1. CNT thin film

4.1.1. Fabrication of CNT thin film

We fabricate CNT-MESFET biosensor using separated semiconducting single-walled nanotube (SC-SWNTs) thin film. Separated SC-SWNTs were prepared magnetic particle assisted separation method and purchased at Nanointigris

[99,100]. We used 3-AminopropyltriethoxySilane (APTES) assisted self assemble method SC-CNTs thin film [101-103]. Fabrication procedure of the APTES-assisted SC-SWNTs film deposition is shown in Fig. 45. We used silicon substrate with 200 nm oxide layers (Si/SiO_2) as substrate and Si substrate was treated by piranha solution (a mixture of sulfuric acid (H_2SO_4) and hydrogen peroxide (H_2O_2), 3:1 volume ratio) for 30 min at 80°C. Piranha treatment is modification of –OH group at the surface of SiO_2. Piranha treatment, the SiO_2 surface has hydrophilic surface. After piranha treated wafer was thoroughly washed with deionized water and dried by blowing N_2.

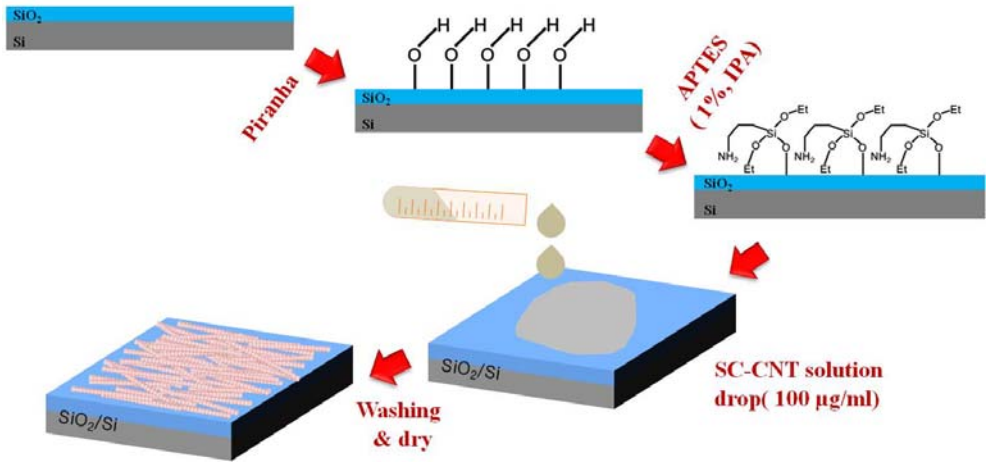

Figure 45. Fabrication procedure of semiconducting nanotube thin film

After wafer drying, cleaned wafers were dipped into an 3-Aminopropyl-triethoxySilane (APTES, 1%, volume ratio with IPA) to form amine terminated

self assemble monolayer (SAM) for 30 min. Wafer was thoroughly washed with 2-propanol and N_2 blown dried. 100 μg/ml of 99 % semiconducting nanotube solution was dropped onto the APTES modified wafer and left for CNT adsorption for 1 hour. After excess nanotube solution was washed with DI water and wafer was N_2 blown and dried. Fig. 46 shows SEM images of the deposited nanotubes film on the Si wafer. The SEM images indicate high density, uniform CNTs film. Acquisition of uniform CNTs film is most important issues concerning the integration of CNTs device.

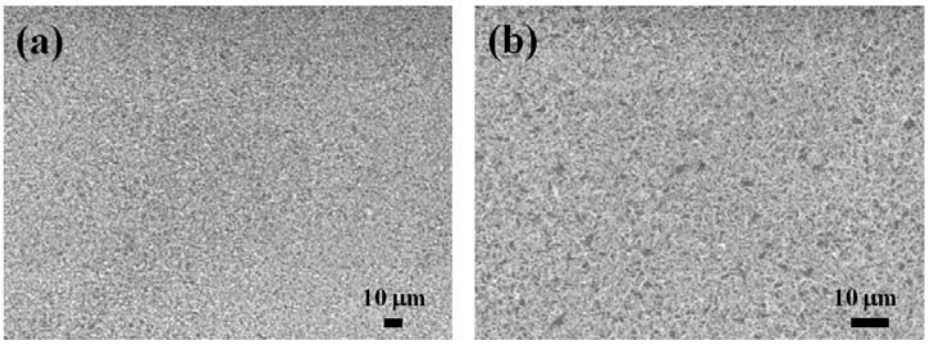

Figure 46. SEM image of the deposited semiconducting SWNTs on the Si/SiO_2 wafer using APTES-assisted deposition.

4.1.2. CNT-FETs array fabrication and Characteristics

Following the nanotube deposition is the device fabrication process. Thermally grown SiO_2 (200 nm) is used back-gate dielectric. The source and drain electrodes are patterned by photolithography, and Cr (30 Å) and Au (500 Å) are deposited using thermal evaporation followed by a lift-off process. Finally, we removed the possible leakage in the devices and precise definition of CNTs channel length/width since the separated nanotube thin film cover the entire substrate. We needed one more step of electron beam lithography for the masking of the CNT channel. By using O_2 plasma, we removed the nanotubes outside the device channel region.

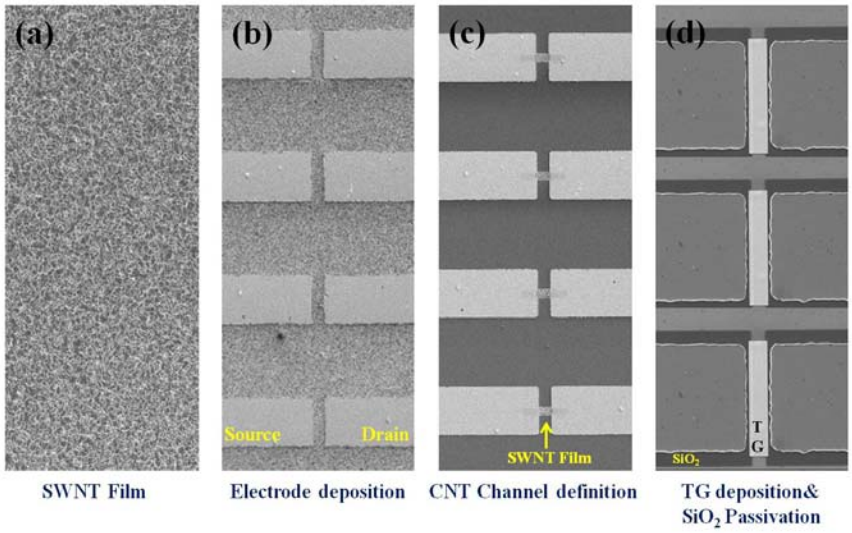

Figure 47. SEM image of CNT-TFTs array fabrication process

Fig. 47 (c) is a SEM image of CNT-TFTs (thin film transistors) array using CNTs thin film. CNT-TFTs are made with channel width (W) of 10 μm, and channel length (L) of 6 μm. Prevention of the unspecific binding of biomolecules at exposed CNTs, we passivated on the exposed CNTs region by SiO_2 using electron beam deposition and lithography (Fig. 47 (d)).

We carried out a study of the electrical performance of the CNT-TFTs. Due to uniform and the high density of CNT nature of the separated semiconducting nanotube thin-film deposited on Si/SiO_2 substrates with APTES functionalization, the CNT-FETs array are also expected to behave uniformly. Fig. 48 is the back gate voltage dependence of (I_{DS}-V_{BG}) characteristics of a typical CNT-FETs array (channel length = 6 μm, and width = 10 μm) of 10 devices. All devices show a typical p-type semiconductor characteristic and obvious on/off state. Moreover I_{DS}-V_{BG} curves are similar to each other. These mean semiconducting CNTs film forms the uniform semiconducting nanotubes network, high density of devices with good performance.

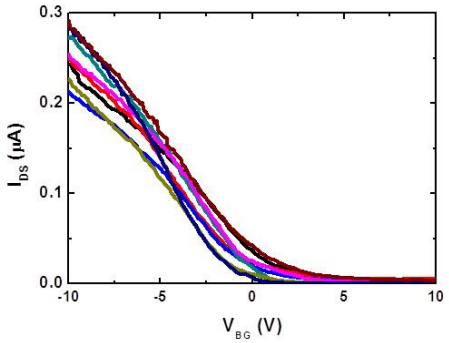

Figure 48. The transfer (I_{DS}-V_{BG}) characteristics of representative 10 devices at the same substrate with V_{DS} = 1 V.

The uniformity of the devices is illustrated in Fig. 49, which shows the on/off ratio and threshold voltage (V_{th}) of 10 representative CNT-TFTs. The on/off ratio exceeds 2×10^4 and the threshold voltage is within the range about 1.5 V with 10 representative CNT-TFTs.

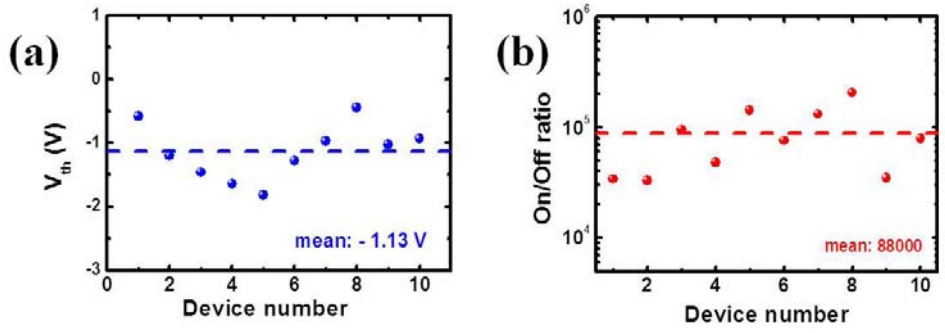

Figure 49. Electronic properties of CNT-FETs array using back gate. (a) Threshold voltage (V_{th}) and (b) on/off ratio of 10 representative CNT-TFTs showing the uniformity of devices. The dashed line represents the average value.

CVD grown nanotube thin-films with mixed nanotubes had also been used to demonstrate TFTs and flexible devices [104-106]. However, the major problem of using CVD grown nanotube networks is the coexistence of metallic and semiconducting nanotubes with approximate 33% nanotubes being metallic characteristic. On the basis of separated nanotubes with 99% semiconducting nanotubes, we have achieved solution-based assembly of separated semiconducting nanotube uniform thin films on large scale substrate. Device fabrication using

APTES assisted self assemble method are achieved high yield, small distribution threshold voltage, high on/off ratios (> 2 × 10^4). This approach can be easily application to fabrication of CNT-FETs array for large scale substrate and reduce the sensor-to-sensor variation.

4.1.3. Experimental details of CNT-MESFET

We studied the specific binding of HRP antibody and antigen using the CNT-MESFET sensor. Before HRP antibody immobilization on the Au top gate, Cys-3 protein G and Z domain of protein A expressed E.Coli outer membrane were modified on the top gate of the CNT-MESFET.

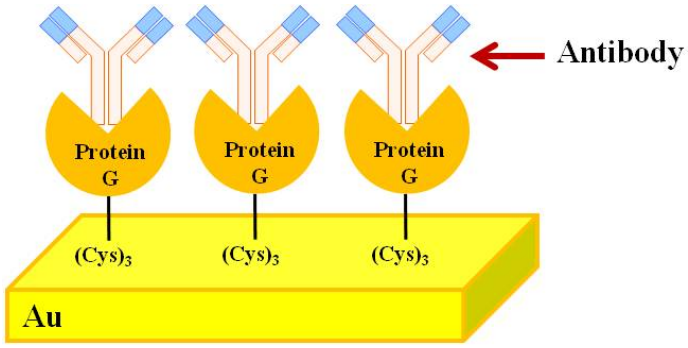

Figure 50. Schematic of self-oriented antibody by protein G

Protein G has been widely used to immobilize various immune system related protein called immunoglobulins because of self-oriented antibody immobilization. The schematic of self-oriented antibody by protein G is displayed in Fig. 50. Each antibody consists of four polypeptides. Two heavy and two light chains joined to form a "Y" shaped molecule (Fig. 51). Light chains are called F_{ab} (fragment antigen binding) and heavy chains are called F_c (fragment crystallizable). To achieve a stable and orientated attachment of immunoglobulin molecules on a solid surface without disrupting biological function (enhance the selectivity and specificity), it is allows to immobilize only the F_c region of the immunoglobulin leaving the F_{ab} domain available to attach the antigen.

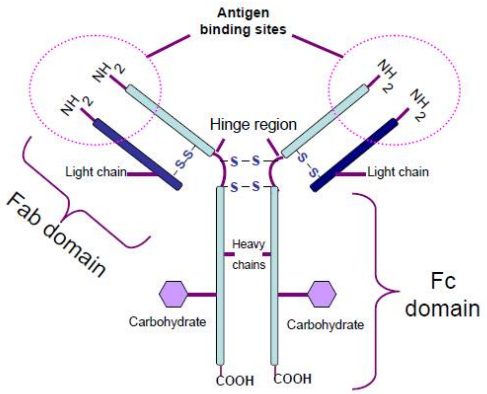

Figure 51. Schematic representation of the immunoglobulin G (IgG)

An approach to find out a well-defined antibody surface is the use of protein G. Therefore, antigen binding domains of antibodies oriented

immobilization is one of the key issues in the development of immunosensors. Protein G allows increasing the density of binding sites available for the antigen and therefore the sensitivity of the biosensors devices. In addition, we used cysteine tagged protein G. Cystein (abbreviated as Cys) is an α-amino acid with the chemical formula $HO_2CCH(NH_2)CH_2SH$. The side chain on cysteine is thiol which can be covalent bind to gold.

Protein A has been used for immunoaffinity layer because of its strong affinity to F_c region of antibodies and F_c region captured antibodies expose F_{ab} region to show higher sensitivity. Z domain of protein A with IgG-binding activity was expressed on the outer membrane of E.coli as a fusion protein of AIDA-1 by using auto display method [107, 108], and the outer membrane with auto displayed Z-domain was applied for the antibody immobilization of the CNT-MESFET biosensor. The outer membrane of E.coli with Z-domain was coated to the gold top gate surface CNT-MESFET sensor (Fig. 52).

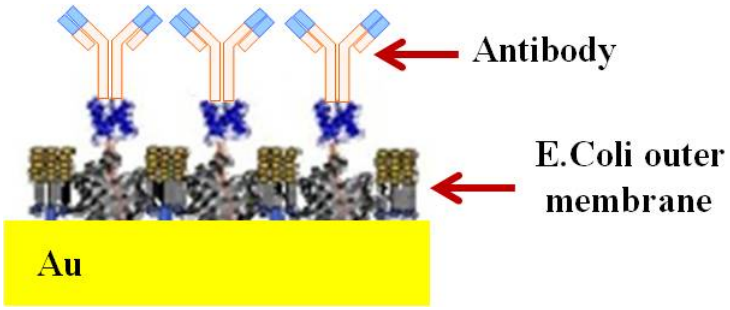

Figure 52. Schematic of outer membrane of E.coli coated on Au surface and after antibody immobilization.

We immobilized HRP antibody at the CNT-MESFET using protein G and E.coli outer membrane (linker). After modification of HRP antibody (5 μg/ml in PBS), various concentration of HRP antigen was injected into the micro fluidic channel. Real-time conductance measurement was conducted at room temperature.

4.2. Results and Discussion

4.2.1. HRP antigen detection using CNT-FET

Horseradish peroxidase (HRP) antigen and antibody specific binding was detected by CNT-FET biosensor based CNT thin film.

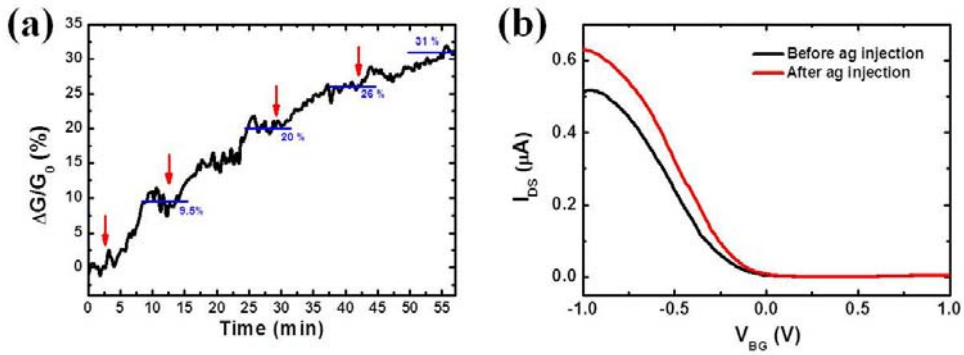

Figure 53. CNT-FET based HRP antigen detection in PBS (a) Real-time response to various concentrations of HRP antigen concentration dependence. Arrow is the points of introduction of HRP antigen (1 pg/ml, 10 pg/ml, 100 pg/ml, and 1 ng/ml). (b) I_{DS}-V_{BG} curve of the CNT-MESFET at the V_{SD} = 0.2 V (Black line is before and red line is after injection HRP antigen).

In this experiment, real-time measurement was conducted during HRP antibody and antigen specific binding in PBS. CNT surface modification details were explained at chapter 2.2.1. After chemical linker incubation, in order to immobilize HRP antibody on the CNT channels, the device was exposed to the 5 μg/ml HRP antibody in PBS for 1 hour at room temperature. After rinsing with PBS, pure PBS was injected into the micro fluidic channel for electrical measurements.

The electrical properties of the CNT-FETs were measured in real-time at room temperature. Fig. 53 (a) shows the real time dependence of after introduction of HRP antigen at various concentrations. Adding the antigen caused a sharp increase in the source and drain current and then a gradual saturation at higher values. After injection of higher concentration of HRP antigen, electrical conductance was increased higher value.

CNT-FET sensor characteristics such as I_{DS}–V_{BG} transfer curves are known to be sensitive to changes in environment around carbon nanotubes, including molecular presence [109]. Transfer characteristics of bare CNT-FET devices are well described in the literature and consistent with p-type with positive threshold voltages [110]. Specific binding of HRP antibody and antigen on the CNT-FET sensor results in a shift of I_{DS}–V_{BG} curve toward more positive gate voltage values (Fig. 53 (b)).

4.2.2. HRP antigen detection using CNT-MESFET

First, we used protein G linker to immobilize the HRP antibody. Fig. 54 (a) is the normalized conductance of the CNT-MESFET after introduction of HRP antigen. Similar to CNT-FET sensor, real-time measurement was conducted during HRP antibody and antigen specific binding in PBS.

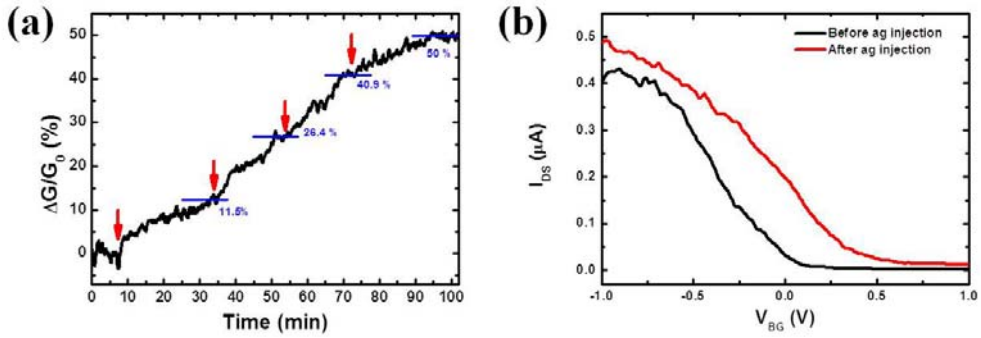

Figure 54. Electrical measurement of CNT-MESFET sensor (a) Real-time dependence of normalized conductance using the CNT-MESFET after injection of various concentration of HRP antigen (linker: protein G, Arrows indicate HRP antigen introduction points of concentrations. 1 pg/ml, 10 pg/ml, 100 pg/ml and 1 ng/ml). (b) I_{DS}-V_{BG} curve of the CNT-MESFET at V_{DS} = 0.3 V (Black line is before and red line is after injection HRP antigen).

HRP antigen injection was caused increase the conductance of the CNT-MESFET. After injection of higher concentration of HRP antigen, electrical conductance was increased higher value. I_{DS}–V_{BG} transfer curve is similar to CNT-

FET. Specific binding of HRP antibody and antigen to the sensor results in a shift of I_{DS}–V_{BG} curve toward more positive gate voltage values (Fig. 54 (b)).

Second, we used the E. coli outer membrane with Z-domain for HRP antibody linker to the CNT-MESFET gold top gate surface. Fig. 55 shows the electrical characteristics of the E.coli outer membrane linker used CNT-MESFET.

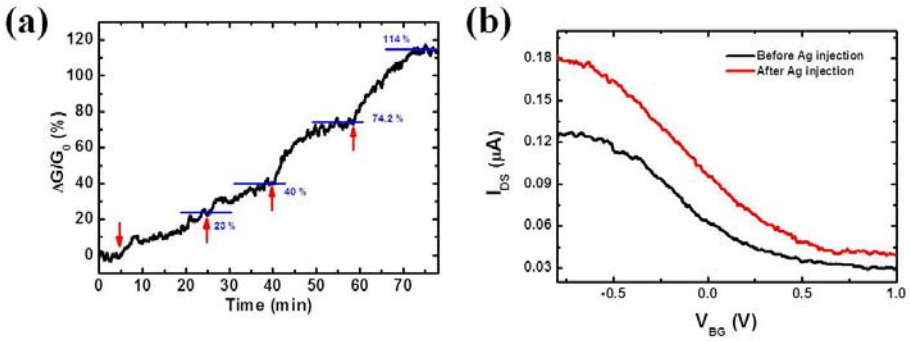

Figure 55. Electrical characteristics of the E. coli outer membrane used CNT-MESFET sensor (a) Real-time monitoring of the CNT-MESFET after the injection of HRP antigen with various concentrations. (Antibody was immobilized using Z-domain expressed E.Coli outer membrane. Arrows indicate the points of introduction of HRP antigen with various concentrations of 1 pg/ml, 10 pg/ml, 100 pg/ml, and 1 ng/ml). (b) I_{DS}-V_{BG} curve of the CNT-MESFET at V_{SD} = 0.5 V (Black line is before and red line is after injection HRP antigen).

In the case of E.coli OM with Z-domain modified CNT-MESFET sensor, HRP antigen injection caused increase the conductance of CNT-MESFET at real-time measurement. I_{DS}–V_{BG} transfer curves also similar to chemical linker used

CNT-FET and protein G modified CNT-MESFET.

We have studied CNT-MESFET biosensors and compared with CNT-FET biosensors. HRP antibody was immobilized on the surface of CNT at CNT-FET biosensors using a chemical linker. The gold top gate surface of CNT-MESFET biosensors was used protein G and outer membrane of E.coli with Z-domain as linker of HRP antibody. Based on the measured data, we calculated the sensitivity base on the 3 kinds of CNT sensors.

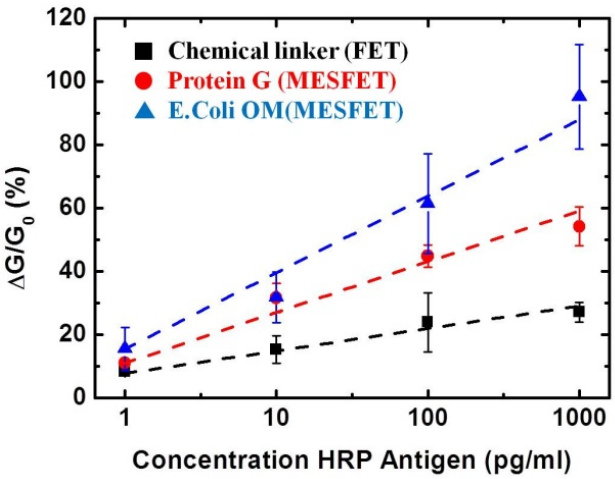

Figure 56. Sensitivity comparison of CNT-FET and CNT-MESFET. Black dashed line represent the CNT-FET sensor using chemical linker, red and blue dashed line indicate the CNT-MESFET sensor using protein G and Z-domain expressed E. coli outer membrane, respectively.

CNT-FET and CMT-MESFET biosensor shows a linear relationship to the HRP antigen concentration and conductance change. In the Fig. 48, CNT-MESFET biosensors provided higher sensitivity than the CNT-FET biosensors. Moreover, higher sensitivity was found with Z-domain expressed E. coli outer membrane linker sensor than the protein G linker sensor.

We compared Au particle number for study the different sensitivity of 3 kinds of sensor using 20 nm diameter Au nanoparticle conjugated secondary antibody.

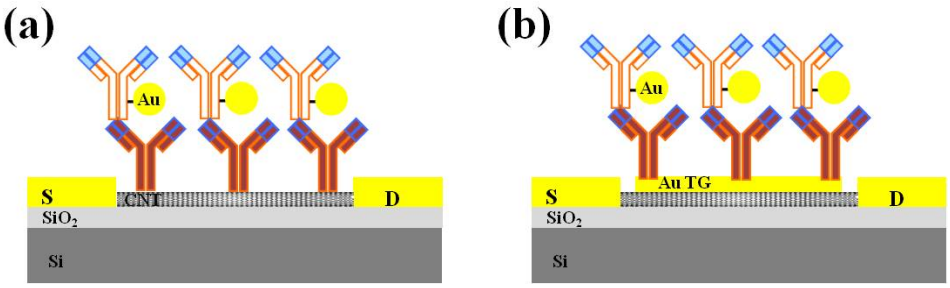

Figure 57. Schematic representation of Au nanoparticle conjugated secondary antibody assembly at the sensor. (a) Au nanoparticle conjugated secondary antibody was immobilized at the surface of CNT at CNT-FET sensor using chemical linker. (b) Au nanoparticle conjugated secondary antibody was immobilized at the surface of gold top gate at CNT-MESFET sensor using protein G and Z-domain expressed E. coli outer membrane linker.

Au nanoparticle conjugated secondary antibody assemble process is as follow. Linker materials were modified at the surface CNT or Au top gate for 1 hour. Anti-goat protein (2 μg/ml, PBS) was introduced for 1 hour at room temperature. After Anti-goat protein assembly, rinsed with blank PBS for remove the unspecific binding protein. Then Au nanoparticle conjugated secondary antibody was assembled for 1 hour at room temperature. For SEM measurement, sample was thoroughly rinsed with PBS and dried with N_2.

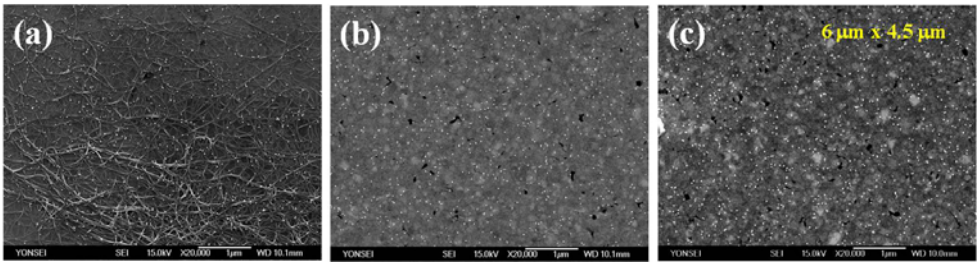

Figure 58. SEM image of 20 nm Au nanoparticles at the (a) immobilized at CNT surface using chemical linker, (b) immobilized at Au top gate surface using protein G and (c) immobilized at Au top gate surface Z-domain expressed E.coli outer membrane. Bright dot is Au nanoparticles.

Fig. 58 is the SEM images of 20 nm Au nanoparticles modified at the CNT surface (by chemical linker) and Au top gate surface (by protein G and E.coli outer membrane with Z-domain). Based on the SEM image, we measured the number of Au particle with same area to 3 cases of linker. In the Fig. 59, chemical linker used CNT-FET sensor show the smallest number of Au nanoparticles.

This is due to the protein G and Z-domain an excellent binding specialty to the F_c region of an IgG antibody and therefore provides proper orientation of the bound antibody, resulting in the antigen binding sites optimally exposed to the assay solution. But chemical linker is random adsorption of the antibody on a surface of CNT.

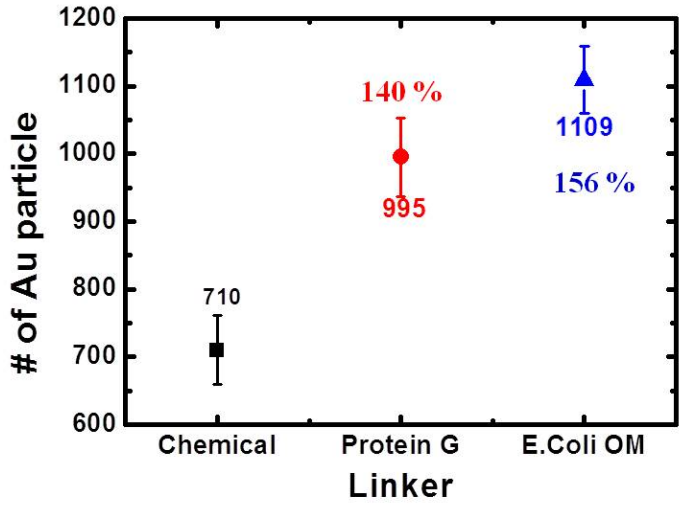

Figure 59. Au particle number comparison of chemical linker, protein G and E.coli outermembrane linker used CNT based sensor

In addition, we have also tested these sensors for HRP antigen spiked in serum to study the feasibility of clinical applications. CNT-MESFET was used for higher sensitivity than CNT-FET. In order to produce selective biosensors, it is necessary to avoid the non-specific binding of possible interferences present in the real samples [111]. Protein assemble process is similar to previous experiment but

bovine serum albumin (BSA) was blocked after HRP antibody assembly. BSA was used to block the nonspecific binding of proteins with the sensing element.

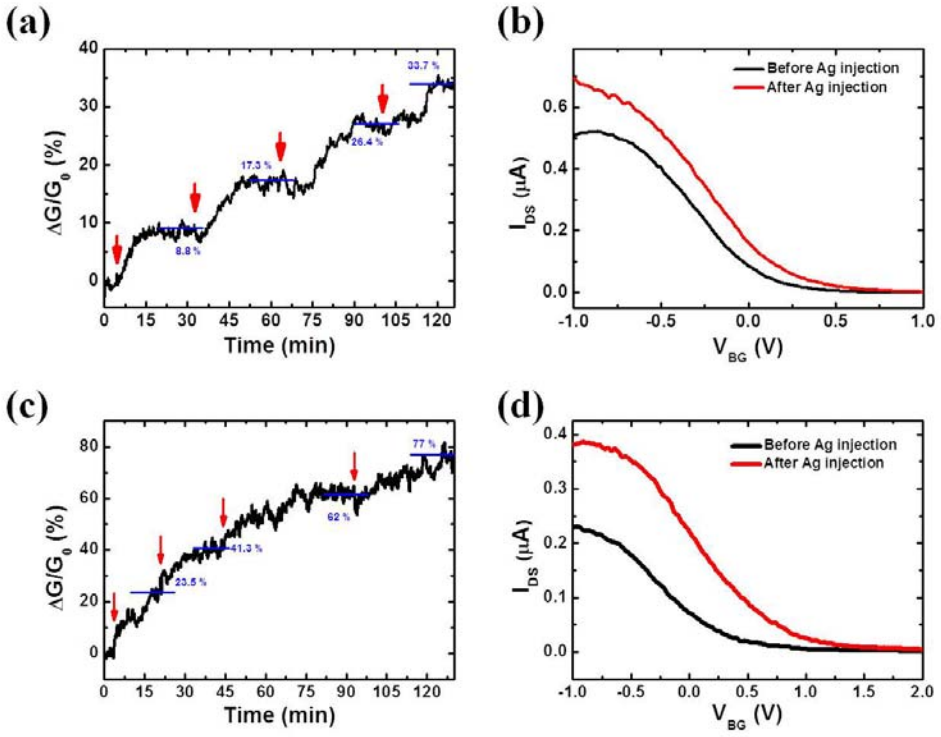

Figure 60. HRP antigen detection of CNT-MESFET in serum (a) Real-time detection of the HRP antigens spiked in serum at various concentrations using CNT-MESFET. HRP antibody was anchored by protein G. Arrows indicate the points of introduction of HRP antigen (1 pg/ml, 10 pg/ml, 100 pg/ml, and 1 ng/ml) (b) I_{DS}-V_{BG} curve of the CNT-MESFET at V_{DS} = 0.5 V (Black line is before and red line is after injection HRP antigen). (c) Real-time detection of the HRP antigens spiked in serum at various concentrations using CNT-MESFET. HRP antibody was immobilized using Z-domain expressed E.Coli outer membrane. Arrows indicate the points of introduction of HRP antigen (1 pg/ml, 10 pg/ml,

100 pg/ml, and 1 ng/ml). (d) I_{DS}-V_{BG} curve of the CNT-MESFET at V_{DS} = 0.5 V (Black line is before and red line is after injection HRP antigen).

In this experiment, HRP antigen was diluted in serum. After BSA assembly, serum was injected into the micro fluidic channel for the acquisition of stable electrical signal. After electrical signal saturation in serum environment, HRP antigen spiked in serum was subsequently injected into the micro fluidic channel.

CNT-MESFET sensor at Fig. 60 (a) and (b) was immobilized HRP antibody using protein G. Fig. 60 (c) and (d) was immobilized the HRP antibody using Z-domain expressed E.Coli outer membrane. Fig. 60 (a) and (c) are the real-time monitoring of electrical conductance after HRP antigen spiked in serum. The introduction of antigen caused the conductance increase. This is also similar to the PBS based CNT-MESFET trend. After the injection of higher concentration of HRP antigen, electrical conductance was increased higher value. I_{DS}–V_{BG} transfer curves also similar to CNT-MESFET in PBS condition. This means HRP antibody and antigen specific binding occur in the serum environment. Specific binding of HRP antibody and antigen, results in a shift of I_{DS}–V_{BG} curve the positive gate voltage region (Fig. 60 (b), (d)).

Fig. 61 is summarized sensitivity of CNT-MESFET biosensors using Z-domain expressed E. coli outer membrane sensor and protein G sensor in serum base. E.coli OM with Z-domain linker used CNT-MESFET sensor shows the higher sensitivity than protein G used sensor in serum base. This is due to the strong affinity Z-domain to the mouse origin HRP antigen than the protein G [112]

and E.coli outer membrane is negatively charged, this charged membrane efficiently prevent the unspecific binding of proteins in serum.

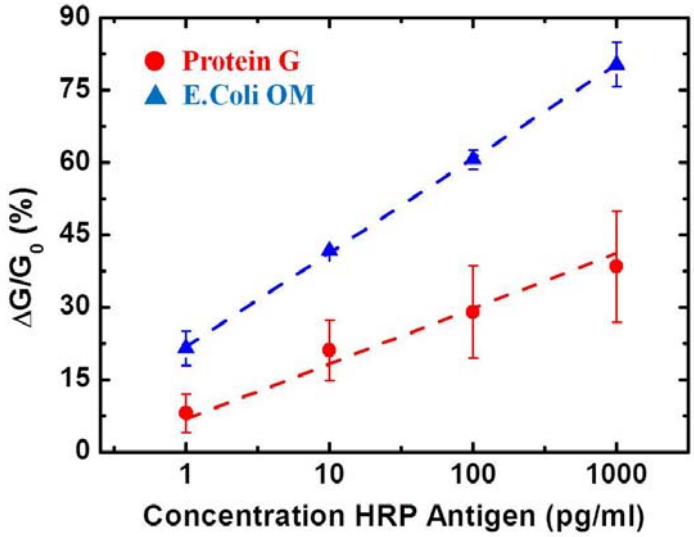

Figure 61. Sensitivity comparison of protein G linker used CNT-MESFET sensor and E.Coli outer membrane with Z-domain linker used CNT-MESFET sensor. Blue dashed line indicate the CNT-MESFET sensor using Z-domain expressed E. coli outer membrane, and red dashed line is protein G linker assembled sensor.

V. Summary

Carbon Nanotube - Based Biosensor for Detection Hepatitis B

We have fabricated CNT biosensors with the FET structure and detected hepatitis B. The metal electrodes were passivated using SiO_2 or SiNx to minimize the contact effects and the micro fluidic channel was mounted on the biosensor. When hepatitis B antigen was introduced into the micro fluidic channel, in which the CNT biosensor with hepatitis B antibody immobilized was mounted, the conductance increase was observed, whereas when BSA was added, no conductance change was found. This result indicates the specificity of the CNT–FET biosensor. We also investigated the concentration dependence of hepatitis B antigen on the conductance and found the linear relationship between the conductance and the concentration in the logarithm scale.

Carbon Nanotube - based dual mode biosensor

We have fabricated a CNT-based biosensor with a MESFET structure to develop a dual-mode biosensor for electrical and SPR measurements. The Au strip, which was deposited on the middle of the CNT channel, acted as the top gate because of the Schottky contact between the Au strip and the CNT. For comparison, we

measured the I_{SD}-V transfer curves for CNT-MESFET, CNT-FET, and CNT-MOSFET. The CNT-MESFET exhibited the steepest transition of I_{SD} because it had the largest liquid gate capacitance among the three devices. DNA hybridization occurring on the Au top gate of CNT-MESFET decreased the I_{SD} of the CNT-MESFET, which can probably be attributed to the change in the effective work function of Au, leading to band bending in the bulk CNT. To measure *I*SD and SPR at the same time, CNT-MESFET with ultra-long CNTs was fabricated on a quartz substrate. DNA hybridization on the Au top gate resulted in a shift in the SPR reflectance minimum as well as the decrease in the I_{SD}. Since SPR measurements provided reproducible results independently of the sensor, these results demonstrated that the sensor-to-sensor variation of conductance measurements might be calibrated using the SPR data.

CNT-MESFET biosensor using CNT thin film

We have developed CNT-MESFET biosensors and compared with CNT-FET biosensors. Horseradish peroxidase (HRP) antibodies were immobilized on the CNT-FET biosensors using a chemical linker, and on the CNT-MESFET biosensors protein G or protein A. Then, HRP antigens were detected by measuring the conductance change in real time. For both CNT-FET and CMT-MESFET biosensors a linear relationship was observed between the antigen concentration and the conductance change in semi-logarithmic scales. However, CNT-MESFET

biosensors provided higher sensitivity than the CNT-FET biosensors. Moreover, higher sensitivity was found with protein A than with protein G. In addition, we have also tested these sensors for HRP antigens spiked in serum to study the feasibility of clinical applications.

VI. Reference

[1] S. Iijima, Nature, 354, 56 (1991)

[2] P. G Collins, P. Avouris, Scientific American, 283, 62 (2000)

[3] S. Fan, M. G. Chapline, N. R. Franklin, T. W. Tombler, A.M. Cassell, H. Dai, Science, 283, 512 (1999)

[4] S. S. Wong, E. Joselevich, A. T. Woolley, C. L. Cheung, C. M. Lieber, Nature, 394, 52 (1998)

[5] T. Rueckes, K. Kim, E. Joselevich, G. Y. Tseng, C. L. Cheung, C. M. Lieber, Science, 289, 94 (2000)

[6] Z. Yao, H. W. C. Postma, L. Balents, C. Dekker, Nature, 402, 273 (1999)

[7] E. T. Thostensona, Z. Renb, T. W. Choua, Composites Science and Technology, 61, 1899 (2001)

[8] R. H. Baughman, A. A. Zakhido v, W. A. de Heer, Science, 297,787 (2002).

[9] M. S. Dresselhaus, G. Dresselhaus, P. C. Eklund, Science of fullerenes and carbon nanotubes. San Diego: Academic Press (1996)

[10] P. M. Ajayan, Chem. Rev., 99, 1787 (1999)

[11] J. W. Mintmire, B. I. Dunlap, C. T. White, Phys. Rev. Lett., 68, 631 (1992)

[12] N. Hamada, S. Sawada, A. Oshiyama, Phys. Rev. Lett., 68, 1579 (1992)

[13] R. Saito, M. Fujita, G. Dresselhaus, M. S. Dresselhaus, Appl. Phys. Lett., 60,

2204 (1992)

[14] Z. Yao, C. Dekker, P. Avouris, Electrical Transport through Single-Wall Carbon Nanotubes, Carbon Nanotubes: Synthesis, Structure, Properties, and Applications, Springer-Verlag GmbH, Heidelberg (2001), Vol.80, p.147.

[15] L. Forro, C. Schonenberger, Physical properties of Multi-wall Nanotubes, Carbon Nanotubes, Topics in Applied Physics, Springer-Verlag, Heidelberg (2001)

[16] P. L. McEuen, J. Y. P ark, MRS Bulletin 29, 272 (2004)

[17] K. Liu, M. Burghard, S. Roth, P. Bernier, Appl. Phys. Lett., 75, 2494 (1999)

[18] S. J. T ans, A. R. M .Verschueren, C.Dekker, Nature 393, 49 (1998)

[19] D. V. Singh, K. A. Jenkins, J. Appenzeller, D. Neumayer, A. Grill, H. S. P. Wong, IEEE Trans. Nanotech., 3, 383 (2004)

[20] V. Derycke, R. Martel, J. Appenzeller , P. A vouris, Appl. Phys. Lett., 80, 2773 (2002)

[21] A. M. Rao, P. C. Eklund, S. Bandow, A. Thess, R. E. Smalley, Nature, 388, 257 (1997)

[22] D. C. J. Sorescu, K. D. Jordan, P. Avouris, J. Phys. Chem. B, 105, 11227 (2001)

[23] R. Czerw, M. Terrones, J. C. Charlier, X. Blase, B. Foley, R. Kamalakaran, N. Grobert, H. Terrones, D. Tekleab, P. M. Ajayan, W. Blau, M. Ruhle, D. L. Carroll, Nano lett., 1, 457 (2001)

[24] H. Dai, Nanotube Growth and Characterization, Topics in Applied Physics, Springer-Verlag, Berlin, 80, 29 (2001)

[25] C. Journet, W. K. Maser, P. Bernier, A. Loiseau, M. Lamyde la Chapelle, S.

Lefrant, P. Deniard, R. Lee, J. E. Fischerk, Nature, 388, 756 (1997)

[26] P. Nikolaev, M. J. Bronikowski, R. K. Bradley, F. Rohmund, D. T. Colbert, K. A. Smith, R. E. Smalley, Chemical Physics Letters, 313, 91 (1999)

[27] Z. F. Ren, Z. P. Huang, D. Z. Wang, J. G. Wen, J. W. Xu, J. H. Wang, L. E. Calvet, J. Chen, J. F. Klemic, M. A. Reed, Applied Physics Letters, 75, 1086 (1999)

[28] Z. F. Ren, Z. P. Huang, J. W. Xu, J. H. Wang, P. Bush, M. P. Siegal, P. N. Provencio, Science, 282, 1105 (1998)

[29] Z. P. Huang, J. W. Xu, Z. F. Ren, J. H. Wang, M. P. Siegal and P. N. Provencio, Applied Physics Letters, 73, 3845 (1998)

[30] A. G. Rinzler, J. Liu, H. Dai, P. Nikolaev, C. B. Huffman, F. J. Rodriguez-Macias, P. J. Boul, A. H. Lu, D. Heymann, D. T. Colbert, R. S. Lee, J. E. Fischer, A. M. Rao, P. C. Eklund, R. E. Smalley, Applied Physics A, 67, 29 (1998)

[31] S. Iijima, T. Ichihashi, Nature, 363, 603 (1993)

[32] D. S. Bethune, C. H. Kiang, M. S. Devries, G. Gorman, R. Savoy, J. Vazquez, R. Beyers, Nature, 363, 605 (1993)

[33] Z. Shi, Y. Lian, F. H. Liao, X. Zhou, Z. Gu, Y. Zhang, S. Iijima, H. Li, K. T. Yue, S. L. Zhang, Journal of Physics and Chemistry of Solids, 61, 1031 (2000)

[34] Y. Saito, K. Nishikubo, K. Kawabata, T. Matsumoto, Journal of Applied Physics, 80, 3062 (1996)

[35] A. Thess, R. Lee, P. Nikolaev, H. Dai, P. Petit, J. Robert, C. Xu, Y. H. Lee, S. G. Kim, A. G. Rinzler, D. T. Colbert, G. E. Scuseria, D. Tomanek, J. E. Fischer, R. E. Smalley, Science, 273, 483 (1996)

[36] Y. Zhang, S. Iijima, Applied Physics Letters, 75, 3087 (1999)

[37] 이영희, 탄소나노튜브의 물성과 응용, Sae Mulli, 51, 84 (2005)

[38] M. Ge, K. Sattler, Applied Physics Letters, 64, 710 (1994)

[39] G. Che, B. B. Lakshmi, C. R. Martin, E. R. Fisher, Chemistry of Materials, 10, 260 (1998)

[40] W. Z. Li, S. S. Xie, L. X. Qian, B. H. Chang, B. S. Zou, W. Y. Zhou, R. A. Zhao, G. Wang, Science, 274, 1701 (1996)

[41] X. X. Zhang, Z. Q. Li, G. H. Wen, K. K. Fung, J. Chen, Y Li, Chemical Physics Letters, 333, 509 (2001)

[42] Y. C. Choi, Y. M. Shin, Y. H. Lee, B. S. Lee, G. Park, W. B. Choi, N. S. Lee, J. M. Kim, Applied Physics Letters, 76, 2367 (2000)

[43] M. Okai, T. Muneyoshi, T. Yaguchi, S. Sasaki, Applied Physics Letters, 77, 3468 (2000)

[44] C. Bower, O. Zhou, Wei Zhu, D. J. Werder, S. Jin, Applied Physics Letters, 77, 2767 (2000)

[45] C. Bower, W. Zhu, S. Jin, O. Zhou, Applied Physics Letters, 77, 830 (2000)

[46] H. Cui, O. Zhou, B. R. Stonera, Journal of Applied Physics, 88, 6072 (2000)

[47] M. Robers, I. J. A. M. Rensink, C. E. Hack, C. E. Aarden, C. P. M. Reutelingsperger, J. F. C. Glatz, W. T. Hermens, Biophys. J, 76, 2769 (1999)

[48] C. J. McNeil, D. Athey, O. H Wah, Biosens Bioelectron, 10, 75 (1995)

[49] A. Nel, T. Xia, L. Mädler, N. Li, Science, 311, 622 (2006)

[50] S. Park, T. A. Taton, C. A. Mirkin, Science, 295, 1503 (2002)

[51] L. He, M. D. Musick, S. R. Nicewarner, F. G. Salinas, S. J. Benkovic, M. J.

Natan, C. D. Keating, J. Am. Chem. Soc. 122, 9071 (2000)

[52] A. D. McFarland, R. P. Van Duyne, Nano Lett. 3, 1057 (2003)

[53] A. P. Graham, G. S. Duesberg, R. V. Seidel, M. Liebau, E. Unger, W. Pamler, F. Kreupl,W. Hoenlein, Small, 1, 382 (2005)

[54] G. Grüner, Anal. Bioanal. Chem. 2006, 384, 322

[55] I. Willner, Science, 298, 2407 (2002)

[56] M. Shim, N. W. S. Kam, R. J. Chen, Y. Li, H. Dai, Nano Letters. 2, 285 (2002)

[57] W. Huang, S. Taylor, K. Fu, Y. Lin, D. Zhang, T. W. Hanks, A. M. Rao, Y. P. Sun, Nano lett. 2, 311 (2002)

[58] J. J. Davis, H. L. H. Green, H. Allen, O. Hill, Y. C. Leung, P. J. Sadler, J. Sloan, A. V. Xavier, S. C. Tsang, Inorg. Chim. Acta, 272, 261 (1998)

[59] F. Balavoine, P. Schultz, C. Richard, V. Mallouh, T. W. Ebbesen, C. Mioskowski, Angew. Chem. Int. Edit, 38, 1912 (1999)

[60] G. R. Dieckmann, A. B. Dalton, P. A. Johnson, J. Razal, J. Chen, G. M. Giordano, E. Munoz, I. H. Musselman, R. H. Baughman, R. K. Draper, J. Am .Chem. Soc, 125, 1770 (2003)

[61] D. S. Larsen, K. Ohta, Q. Xu, M. Cyrier, G. R. Fleming, J. Chem. Phys. 114, 8008 (2001)

[62] A. Xie, A. F. G. van der Meer, R. H. Austin, Phys Rev Lett. 88, 018102 (2002)

[63] M. Arai, T. Ikura, G. V. Semisotnov, H. Kihara, Y. Amemiya, K. Kuwajima, J. Mol. Biol. 275, 149 (1998)

[64] L. Pollack, M. W. Tate, A. C. Finnefrock, C. Kalidas, S. Trotter, N. C. Darnton, L. Lurio, R. H. Austin, C. A. Batt, S. M. Gruner, S. G. J. Mochrie, Phys. Rev. Lett.

86, 4962 (2001)

[65] K. Kuwata, R. Shastry, H. Cheng, M. Hoshino, C. A. Batt, Y. Goto, H. Roder, Nature Struct. Biol. 8, 151 (2001)

[66] C. M. Jones, E. R. Henry, Y. Hu, C. Chan, S. D. Luck, A. Bhuyan, H. Roder, J. Hofrichter, W. A. Eaton, Proc Natl. Acad. Sci. USA, 90, 11860 (1993)

[67] M. Lim, T. A. Jackson, P. A. Anfinrud, J. Biol. Inorg. Chem. 2, 531 (1997)

[68] E. A. Lipman, B. Schuler, O. Bakajin, W. A. Eaton, Kinetics, 310:1233 (2003)

[69] S. Rosenblatt, Y. Yaish, J. Park, J. Gore, V. Sazonova, P. L. McEuen, Nano Lett. 2, 869 (2002)

[70] A. Star, J. C. P. Gabriel, K. Bradley, G. Gruner, Nano lett. 3, 459 (2003)

[71] R. J. Chen, S. Bangsaruntip, K. A. Drouvalakis, N. W. S. Kam, M. Shim, Y. M. Li, W.Kim, P. J. Utz, H. Dai, J. Proc. Natl. Acad. Sci. USA, 100, 4984 (2003)

[72] K. Besteman, J. O. Lee, F. G. M. Wiertz, H.A. Heering, C. Dekker. Nano Lett. 3, 727 (2003)

[73] J. Homola, Analytical and Bioanalytical Chemistry, 377, 528 (2003)

[74] E.N. Economou, Physical Review, 182, 539 (1969)

[75] M. A. Cooper, Nature reviews, 1, 515 (2002)

[76] J. Kong, H. T. Soh, A. M. Cassell, C. F. Quate, H. Dai, Nature, 395, 878 (1998)

[77] T. Thorsen, S. Maerkl, S. Quake, Science, 298, 580 (2002)

[78] D. Erickson, D. Li, Analy. Cham. Acta. 507, 11 (2004)

[79] R. J. Chen, Y. Zhang, D. Wang, H. Dai, J. Am. Chem. Soc. 123, 3838 (2001)

[80] C. Li, M. Curreli, H. Lin, B. Lei, F. N. Ishikawa, R. Datar, R. J.Cote, M. E. Thompson, C. Zhou, J. Am. Chem. Soc. 127, 12484(2005)

[81] F. Patolsky, G. Zheng, C. M. Lieber, Nature Protocols 1, 1171 (2006)

[82] K. Maehashi, T. Katsura, K. Kerman, Y. Takamura, K. Matsumoto, E. Tamiya, Anal. Chem. 79, 782 (2007)

[83] R. J. Chen, H. C. Choi, S. Bangsaruntip, E. Yenilmez, X. Tang, Q. Wang, Y. L. Chang, H Dai, J. Am. Chem. Soc. 126, 1563 (2004)

[84] S. H. Hwang, H. B. Oh, H. S. Kim, E. Y. Lee, Korean J. Lab. Maed. 26, 436 (2006)

[85] H. Henning, I. Puchta, J. Luhn, P. Schlenke, S. Goerg, H. Kirchner, Blood 100, 237 (2002)

[86] B. P. Nelson, T. E. Grimsrud, M. R. Liles, R. M. Goodman, R. M. Corn, Anal. Chem. 73, 1 (2001)

[87] X. D. Su, Y. J. Wu, W. Knoll, Biosens. Bioelectron. 21, 719 (2005)

[88] S. M. Sze, Physics of Semiconductor Devices, 2nd ed.; Wiley, New York, (1981)

[89] A. J. Bard, L. R. Faulkner, Electrochemical Methods, Fundamentals and Applications, 2nd ed.; Wiley, New York, (2001)

[90] I. Heller, J. Kong, K. A. Williams, C. Dekker, S. G. Lemay, J. Am. Chem. Soc. 128, 7353 (2006)

[91] X. C. Dong, C. M. Lau, A. Lohani, S. G. Mhaisalkar, J. Kasim, Z. X. Shen, X. N. HO, J. A. Rogers, L. J. Li, Adv. Mater. 20, 2389 (2008)

[92] A. Star, E. Tu, J. Niemann, J. Gabriel, C. S. Joiner, C. Valcke, Proc. Natl. Acad. Sci. USA 103, 921 (2006)

[93] D. C. Hansen, K. M. Hansen, T. L. Ferrell, T. Thundat, Langmuir 19, 7514

(2003)

[94] X. W. Tang, S. Bansaruntip, N. Nakayama, E. Yenilmez, Y. L. Chang, Q. Wang, Nano Lett. 6, 1632 (2006)

[95] L. X. Zheng, M. J. O'Connell, S. K. Doorn, X. Z. Liao, Y. H. Zhao, E. A. Akhadov, M. A. Hoffbauer, B. J. Roop, Q. X. Jia, R. C. Dye, D. E. Peterson, S. M. Huang, J. Liu, Y. T. Zhu, Nat. Mater. 3, 673 (2004)

[96] B. H. Hong, J. Y. Lee, T.Beetz, Y. M. Zhu, P. Kim, K. S. Kim, J. Am. Chem. Soc. 127, 15336 (2005)

[97] L. M. Huang, B. White, M. Y. Sfeir, M. Y. Huang, H. X. Huang, S. Wind, J. Hone, S. O'Brien, J. Phys. Chem. B 110, 11103 (2006)

[98] X. D.Su, Y. J.Wu, R. Robelek, W. Knoll, Langmuir 21, 348 (2005)

[99] H. J. Kim, S. Hwang, J. Oh, Y. W. Chang, E. K. Lim, S. Haam, C. S. Kim, and K. H. Yoo, Nanotechnology 22, 045703 (2011)

[100] M. S. Arnold, A. A. Green, J. F. Hulvat, S. I. Stupp, M. C. Hersam, Nature Nanotech. 1, 60 (2006)

[101] C. Wang, J. Zhang, K. Ryu, A. Badmaev, L. G. D. Arco, C. Zhou, Nano lett. 9, 4285 (2009)

[102] N. Rouhi , D. Jain , K Zand , P. J. Burke, Adv. Mater. 23, 94 (2011)

[103] C. Wang, J. Zhang, C. Zhou, ACS nano 4, 7123 (2010)

[104] E. Artukovic, M. Kaempgen, D. S. Hecht, S. Roth, G. Gruner, Nano Lett, 5, 757 (2005)

[105] F. Ishikawa, H. Chang, K. Ryu, P. Chen, A. Badmaev, G. Shen, C. Zhou, ACS nano 73, 73 (2008)

[106] Q.Cao, H. S.Kim, N. Pimparkar, J. P. Kulkarni, C. Wang, M. Shim, K.Roy, M. A. Alam, J. A. Rogers, Nature 454, 495 (2008)

[107] J. Jose, R. Bernhardt, F. Hannemann, J. Biotechnol, 95, 257 (2002)

[108] J. Jose, J. W. Chung, B. J. Jeon, R. Maas, C. H. Nam, J.C. Pyun, Biosens Bioelectron, 24, 1324 (2009)

[109] J. Kong, N. R. Franklin, C. Zhou, M. Chapline, S. Peng, K. Cho, H.Dai, Science 287, 622 (2000)

[110] E. S. Snow, J. P. Novak, P. M. Campbell, D. Park, Appl. Phys. Lett. 82, 2145 (2003)

[111] S. Mao, G. Lu, K. Yu, J. Chen, Carbon, 48, 479 (2010)

[112] L. Bjorck, G. Kronvall, J. Immuunol. 133, 969 (1984)

Publication list

[1] Magnetic nanoparticle-based separation of metallic and semiconducting carbon nanotubes, Hyung Joon Kim, Sungsic Hwang, **Jeseung Oh**, Young Wook Chang, Eun-Kyung Lim, Seungjoo Haam, Chul Sung Kim and Kyung-Hwa Yoo, Nanotechnology, 22, 045703 (2011)

[2] Carbon Nanotube-Based Dual-Mode Biosensor for Electrical and Surface Plasmon Resonance measurements, **Jeseung Oh**, Young Wook Chang, Hyung Joon Kim, Seunghwan Yoo, Dong Jun Kim, Seongil Im, Young June Park, Donghyun Kim and Kyung-Hwa Yoo, Nano Lett. 10, 2755 (2010)

[3] Carbon nanotube-based biosensor for detection hepatitis B, **Jeseung Oh**, Seunghwan Yoo, Young Wook Chang, Kookjin Lim and Kyung-Hwa Yoo, Current Applied Physics, 9, e229, 2009.

[4] Carbon nanotube-based biosensor for detection of matrix metallopeptidase-9 and S-100B, Hyoung-Sub Lee, **Jeseung Oh**, Young-Wook Chang, Yoon-Jung Park, Jeon-Soo Shin and Kyung-Hwa Yoo, Current Applied Physics, 9, e270, 2009.

[5] Electrically refreshable carbon-nanotube-based gas sensors, YoungWook Chang, **Jeseung Oh**, Seung Hwan Yoo, Hyang Hee Choi and Kyung-Hwa Yoo, Nanotechnology, 18, 435504, 2007.

국문 요약

이중모드 측정이 가능한 고감도 탄소나노튜브 바이오센서

기존의 탄소나노튜브 기반의 전계효과형 트랜지스터 구조의 바이오센서보다 향상된 감도를 나타냄과 동시에 바이오센서의 신뢰도 향상을 위해 이중모드 측정이 가능한 탄소나노튜브 기반의 바이오센서를 제작, 그 특성에 관하여 연구를 하였다. 실리콘 기판을 이용하여 리소그래피 방법과 열 증착 방법을 이용하여 소스전극과 드레인 전극을 제작하여 실리콘 기판을 게이트 전극으로 사용하는 전계효과형 트랜지스터 구조의 바이오센서를 구현하여 항원과 항체간의 특이적인 결합에서 전하를 가지고 있는 항원이 결합함에 따라 탄소나노튜브 표면에서의 포텐셜의 변해 나타나는 탄소나노튜브 전계효과형 구조의 바이오센서의 전기 전도도의 변화를 측정하였다. 그리고 탄소나노튜브 바이오센서의 민감도 향상 및 탄소나노튜브 전계효과형 바이오센서의 단점인 부족한 재현성을 향상 시키기 위하여 전기신호와 광 신호 두 종류의 신호를 동시에 실시간으로 측정을 할 수 있도록 탄소나노튜브 채널 가운데 부분에 상부 금 게이트를 제작하여 금속-반도체 전계효과형 트랜지스터 구조의 바이오센서를 제작 한 후, 상부 금 게이트 부분에서 항체를 고정한 후 항원을 주입하여 항원과 항체 간의 특이적 결합에 의해 바뀌는 전기 전도도의 변화를 측정하여 금속-반도체 전계효과형 트랜지스터 구조의 바이오센서의 유효성을 확인 하였다. 그리고 투명한 quartz 기판에 금속-반도체 전계효과형

트랜지스터 구조의 바이오센서를 제작하여 표면 플라즈몬 공명 신호를 측정함과 동시에 소스-드레인 전극을 이용하여 전기 전도도를 측정하여 이중모드 측정을 하였는데 항원과 항체간의 특이적 결합이 일어날 때 전기 전도도의 변화와 표면 플라즈몬 공명 신호를 동시에 실시간으로 측정을 하여 이중 모드 측정도 가능한 것에 대하여 연구를 하였다. 이는 전기 전도도 측정 방법의 장점인 높은 감도를 가지며 광 신호 측정 방법의 장점이 높은 신뢰성을 동시에 가지는 금속-반도체 전계효과형 트랜지스터 구조의 바이오센서를 구현할 수 있었다. 마지막으로 전계효과형 트랜지스터 구조의 바이오센서 와 금속-반도체 전계효과형 트랜지스터 구조의 바이오센서의 민감도 비교를 전기 전도도 측정 방식을 이용하여 연구를 하였는데 금속-반도체 전계효과형 트랜지스터 구조의 바이오센서의 상부 금 게이트 부분의 액체 속에서의 높은 게이트 캐패시턴스와 금 부분에 생체물질들을 고정하는 것이 탄소나노튜브 표면에 고정하는 것보다 더욱 안정적으로 고정을 할 수 있어 전계효과형 트랜지스터 구조의 바이오센서 보다 금속-반도체 전계효과형 트랜지스터 구조의 바이오센서가 높은 민감도를 보이는 것을 연구 하였다.

이를 바탕으로 투명기판에 금속-반도체 전계효과형 구조의 바이오센서를 구현하여 이중 모드 측정이 가능하며 뛰어난 민감도 와 높은 신뢰도를 갖는 바이오센서의 구현이 가능하였다.

핵심어: 탄소나노튜브, 바이오센서, 전계효과형 트랜지스터, 금속-반도체 전계효과형 트랜지스터, 이종모드측정, 표면 플라즈몬 공명, DNA 상보결합, B 형 간염